International Journal of Nanomedicine

Dovepress
Taylor & Francis Group

Open Access Full Text Article

ORIGINAL RESEARCH

Antibacterial and Antitumor Application of Carbon Dots Based on Natural Products for Photodynamic/Photothermal Effects

María P Romero[1], Karina J Lagos[1], Coralia Fabiola Cuadrado[1], Cristina C Garzón-Romero[2], Mateo A Salazar[2], Guillermo Solorzano[3], Jules A Gardener[4], Myriam A González[1], Miryan Rivera[2]

[1]Escuela Politécnica Nacional, Departamento de Materiales, Quito, 170143, Ecuador; [2]Faculty of Exact and Natural Sciences, Pontifical Catholic University of Ecuador (PUCE), Quito, Ecuador; [3]School of Engineering and Applied Sciences (SEAS), Harvard University, Cambridge, MA, USA; [4]Center for Nanoscale Systems (CNS), Harvard University, Cambridge, MA, USA

Correspondence: María P Romero, Email maria.romerom@epn.edu.ec

Introduction: This work presents an easy one-pot synthesis to prepare carbon dots (CDs) from natural products, and their successful application as photosensitizers (PS) and photothermal agents (PA) to combat bacteria and cancerous cells. Despite some differences may appear in the natural extracts due to the obtaining process, it was possible to obtain antibacterial/antitumor photoactivated nanomedicine from common carbon sources as annatto, cinnamon and curcumin.

Methods: Water dispersions of *Bixa Orellana L.* (annatto), *Cinnamomum verum J. Presl* (cinnamon), *Curcuma longa L.* (turmeric or curcumin), and sucrose were used as precursors to prepare CDs1, CDs2, CDs3, and CDs4, correspondingly. The microwave-assisted route was selected to synthesize CDs since it is a simple-timesaving procedure that allows harnessing eco-friendly precursors. The shape, size, and chemical composition of CDs were determined by transmission electron microscopy (TEM), dynamic light scattering (DLS), Fourier-transform infrared (FTIR) and Raman spectroscopies, respectively. In addition, photodynamic, photothermal, luminescence, cytotoxicity, antimicrobial and antitumor analyses were carried out and assessed.

Results and Discussion: This research synthesized irregular shaped CDs, in the range of 2.3 to 3.7 nm, from natural sources. Regarding, their photodynamic and photothermal properties, it was demonstrated that after irradiation CDs generated $^1O_2$ species and the temperature can raise in the range to 40–50 °C, respectively. The antimicrobial capacity of the CDs was tested against microorganism *methicillin-resistant S. aureus* (*MRSA*) and *Extended-Spectrum β-Lactamase* (*ESBL*)*-producing E. coli*. CDs1, CDs2, and CDs3 showed excellent antibacterial effects since complete inhibitions were observed after irradiation with blue light (450 nm; 40 $mW \cdot cm^{-2}$). In addition, the positive antitumor effect was also evidenced against T47D cells. Therefore, it has been demonstrated that the CDs synthesized from green carbon sources such as annatto, cinnamon and curcumin have potential applications as antibacterial and antitumor nanomaterials.

Keywords: carbon-based nanomaterials, microwave-assisted synthesis, bio-inspired route, photosensitizers and photothermal agents

Introduction

CDs comprise zero-dimensional (0D) quasi-spherical nanomaterials with sizes below 10 nm.[1,2] These materials exhibit remarkable properties such as low-cost, biodegradability, photo and chemical stability, fluorescence, and a strong capacity for light absorption.[3–5] These and more interesting characteristics have promoted their thorough study since 2004, when they were first reported.[6] Less than 250 CD-related works were published that year. Nevertheless, the number of studies significantly increased in 2018, almost twenty times higher.[7] Therefore, CDs have been employed in several fields like solar cells,[8] catalysis,[9] metal sensing,[10] biological sensing,[11] drug delivery,[12] bioimaging,[13,14] and so on, owing their versatile and tunable optical and physicochemical properties.[15,16]

Several routes, either top-down or bottom-up, have been employed to prepare CDs.[17–19] Within this subject, the microwave-assisted method under the bottom-up approach is gaining rapt attention since it consists of a direct synthesis,

Received: 20 November 2024
Accepted: 29 March 2025
Published: 19 June 2025

also called one-pot or single-step synthesis.[20] This route only requires a few minutes because microwave irradiation induces faster rates of chemical reactions.[7] In addition, it allows more uniform heating, which often diminishes the formation of by-products and simplifies the purification steps.[21] Likewise, bio-inspired trends that employ natural green precursors have complemented the microwave-assisted route.[22] Carbon-containing sources from parts of plants such as peels, herbs, roots, leaves, flowers, and fruit can be harnessed as bio-starting materials by this cost-effective methodology.[23–25] These natural products are rich in organic compounds that can provide surface functional groups with antimicrobial and anticancer properties.[26–30] The most common functional groups identified in the CD surface comprise N-H, C=O, -OH, -COOH, C-N, and C-O.[31,32] Besides, the organic molecules can contribute as stabilizing, reducing or capping agents.[33] Considering that these species have heteroatoms, the obtained CDs are mainly constituted not only by carbon (C) and oxygen (O) but also by nitrogen (N) or sulfur (S).[34–36] Nonetheless, it is a fact that the final CD characteristics depend on the synthesis conditions and the precursor nature. Regarding the latter, its specific composition directly impacts the CDs.[37]

This study used annatto, cinnamon, and curcumin as natural carbon sources regarding their antimicrobial activities, for example that of the annatto has been attributed to phytochemicals alkaloid, phenol, tannins, saponins, mono, and sesquiterpenes.[38,39] The antimicrobial property of cinnamon is based on bioactive phytochemicals such as cinnamaldehyde and eugenol.[40] Turmeric has been demonstrated that its main components, curcumin and curcumin derivatives, also present antioxidant, anti-inflammatory, antiviral, antifungal, and antimalarial activities.[41,42]

It is important to note that this trend of using natural extracts to synthesize CDs is not new. Several works have proposed the preparation of CDs from these kinds of extracts, for example, from leaves of bamboo or paradise tree, flowers of Magnolia liliiflora, and food like tomato and Solanum lycopersicum,[43–45] among others.

Regarding CD properties of author interest, they exhibit strong optical absorption, ie, when irradiated by a light source in the ranges of UV, visible, or even NIR, they emit light and possess tunable excitation/emission properties.[46,47] The emission response will depend on the CDs' specific features, such as size, composition, presence of surface functional groups, and doping degree. Nevertheless, it is worth noting that the CD emission is also influenced by environmental conditions (temperature, pH, etc.).[47] The irradiated CDs reach an excited state that can generate reactive oxygen species (ROS), heat, or both.[48,49] Consequently, CDs have been considered excellent candidates as photosensitizers (PS) and photothermal agents (PA) within photodynamic (PDT) and photothermal (PTT) therapies, correspondingly.[50] Several authors have focused on this field; thus, CDs have been employed by PDT and PTT to combat bacteria and cancerous cells since these photo-activated techniques are considered low side effects and minimally invasive.[51,52]

With respect to bacteria, they can cause severe infectious diseases and even death if not treated correctly.[53,54] The main challenge in fighting these microorganisms is their drug resistance, which is triggered by the overuse of antibiotics.[55] Hence, conventional treatments become ineffective and require higher doses or repeated administration of drugs, which could increase the risk of unwanted side effects.[56] *Resistant Staphylococcus aureus* (*S. aureus*) and *Escherichia coli* (*E. coli*) are the two main causes of healthcare-associated infections.[55] For example, De Kraker et al determined high excess mortality associated with infections produced by *methicillin-resistant S. aureus* and third-generation *cephalosporin-resistant E. coli*.[57] Thus, the impacts that antibiotic-resistant infections cause on health systems have concerned several researchers and have motivated the exploration of alternative treatments against bacteria.[58–65] In this context, the application of CDs within PDT/PPT has emerged as a novel solution. Yan et al and Wen et al demonstrated that a CD nanocomposite (N, S-CDs with curcumin) presented PDT and PTT properties triggered by a dual-wavelength illumination (808 and 405 nm).[66,67] In addition, these nanocomposites showed excellent biocompatibility since they exhibited low cytotoxicity and negligible hemolytic activity. The researchers conducted successful antibacterial tests against *E. coli* and *S. aureus* (61,62), concluding that N-CDs and curcumin showed great potential in a multimodal PDT synergistic PTT treatment platform. Likewise, Mei et al prepared a nanocomposite of chitosan oligosaccharide functionalized with graphene quantum dots. They proved that three types of antibacterial activity: photodynamic, photothermal, and chemical can kill Gram-positive and Gram-negative bacteria at the same time under irradiation. This combination was also confirmed by treatment of a bacteria-infected wound of a rat.[68] With the same

purpose, Lv. et al synthesized a nanocomposite with methylene blue and carbon quantum dots, concluding that these results encourage the usage of CDs in clinical applications.[60,69]

On the other hand, regarding antitumor applications of CDs, it must be highlighted that cancer comprises a threat to human life. In 2020, ~10 million deaths were reported worldwide by the International Agency for Research on Cancer. According to Miller et al, the most prevalent cancers are breast, uterine corpus, and colon and rectum among females, while prostate, skin melanoma, and colon and rectum among males.[70] Generally, cancer diseases are treated by aggressive procedures such as surgery, radiation, and systemic treatment, which comprise immunotherapy, chemotherapy, targeted and hormonal therapies. Nevertheless, more targeted and less toxic treatments like PDT and PTT, which exhibit reduced long-term morbidity, have also been proposed to fight this illness.[71] In PDT, the abnormal cells could be inhibited by apoptosis, necrosis, or autophagy when ROS are generated, whereas in PTT, the cancerous cells are destroyed by hyperthermia owing to their low tolerance to heat.[72] To cite a few examples, the study by Yue et al prepared an injectable hydrogel by adding nitrogen-rich CDs (N-CDs). They proved that the N-CDs acted as a PS and an efficient cross-linking agent to form a hydrogel network. Besides, after a laser irradiation of 660 nm, the hydrogel showed a high antitumor effect, referring to the in vitro and in vivo experiments.[73] Likewise, Zhang et al prepared a biodegradable poly(γ-glutamic acid) along with glucose oxidase and CDs for simultaneous PDT and PTT under 730 nm laser irradiation. This composite showed a long retention time at the tumor acidic microenvironment and could further target cancer cells. The authors concluded that it is a promising approach for metastasis inhibition.[74] Thus, several related studies have been carried out in recent years. Lagos et al prepared a review summarizing the main results of some carbon-based materials, including CDs, within PDT and PTT applied to destroy tumors.[52]

In this manner, PDT and PTT have become desirable therapeutic approaches to battle bacteria and cancerous cells using a variety of PS and PA, respectively. Among these materials are the CDs.

In this work, different CDs were synthesized from water dispersions of natural carbon sources: (i) *Bixa Orellana L*. (annatto-herbarium collection code QCA237394, identified by botanist Dr. Álvaro J. Pérez), (ii) *Cinnamomum verum J. Presl* (cinnamon - this specie is native to tropical Asia, especially Sri Lanka. It is not native to Ecuador. Although it is possible that specimens of this species exist in Ecuadorian botanical collections, no specific information on its presence was found in the National Herbarium of Ecuador), (iii) *Curcuma longa L*. (turmeric or curcumin - herbarium collection code QCA238186, identified by the botanist Dr. Álvaro J. Pérez) and (iv) sucrose. The nanomaterials obtained in this study were called as CDs1, CDs2, CDs3, and CDs4, from annatto, cinnamon, curcumin, and sucrose, respectively. The shape and size of all the CDs were studied by transmission electron microscopy (TEM). The hydrodynamic diameter was determined by dynamic light scattering (DLS), and the chemical composition, referring to CD functional groups, was analyzed by Fourier-transform infrared (FTIR) and Raman spectroscopies. Luminescence emission measurements were also carried out. Besides, the cytotoxicity, photodynamic and photothermal capacities, along with the antibacterial and antitumor properties were also assessed.

Materials and Methods

Synthesis of CDs

CDs were prepared in an open-vessel microwave (General Electric microwave model JES70W) using simple dispersions based on natural products such as annatto, cinnamon, curcumin, and sucrose. First, 100 g of each natural product was poured and mixed into 150 mL of deionized water. Then, the dispersions were irradiated in a microwave with an energy power of 700 watts for 7 min. The color of the liquid changed from colorless to pale yellow, strong yellow, and pale brown, indicating the formation of CDs.[75] Then, CDs were then purified by repeated dialysis in ultrapure water for two days (double dialysis bag molecular weight 1300 Da). Lastly, the solutions were dried in a hot-air oven to obtain the CDs and then they were stored at 4 °C in the refrigerator before being used in further experiments.

Characterization of CDs (Shape, Size, Zeta Potential and Chemical Composition)

This work's synthesized CDs were characterized using TEM at 200 kV (Jeol ARM field-emission probe-corrected operating in Transmission and Scanning-Transmission modes) to determine their shape, size and crystalline state. The

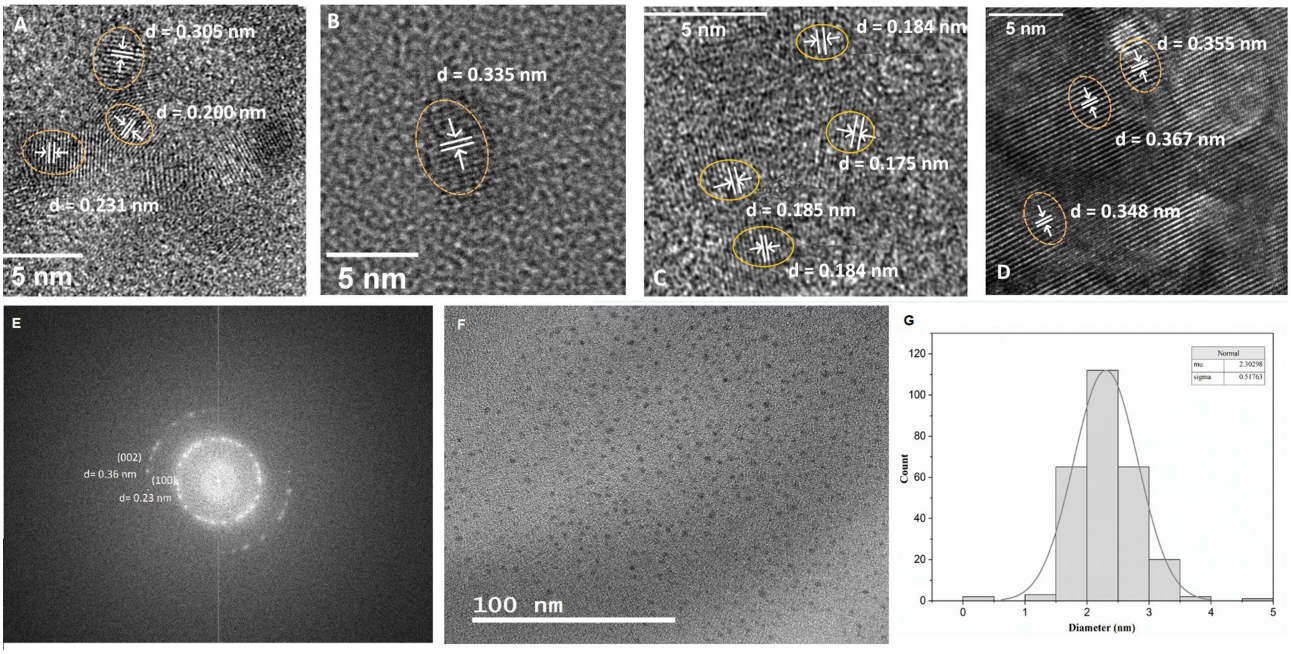

Figure 1 High-resolution TEM images of the synthesized CDs: (**A**) CDs1, (**B**) CDs2, (**C**) CDs3, (**D**) CDs4. Additionally, CDs2 were characterized: (**E**) SAED pattern, (**F**) bright field TEM images and (**G**) size distribution. (d=distance).

particle sizes shown in Figure 1 were measured using the ImageJ software, individual particles were identified and analyzed using the software's particle analysis tool, and the size distribution was obtained by compiling the data. DLS determined the hydrodynamic diameters of the CDs. For this, 1 $mg{\cdot}mL^{-1}$ dispersions were prepared with deionized water, and a Particle Size Analyzer (Brookhaven Instruments Corporation, 90Plus) was used. The same dispersions and equipment described for DLS were employed to determine the ZP. Fourier Transform Infrared-FTIR (Perkin Elmer, Spectrum 100) and Raman (Horiba, LabRAM HR Evolution) spectroscopies were used to analyze the chemical composition. FTIR spectra were acquired in the 4000–500 cm^{-1} range, while Raman spectra were recorded between 1000 and 2000 cm^{-1}.

Luminescence of CDs

The luminescence emission measurements were performed on a Cary Eclipse, Agilent technology spectrofluorometer. The employed concentration of CDs was $50\mu g{\cdot}mL^{-1}$.

Photodynamic Activity and Evaluation of Singlet Oxygen

The photodynamic activity of CDs was assessed by monitoring the oxidation of TMB in the presence of hydrogen peroxide (H_2O_2) using UV-Vis spectroscopy at 652 nm under blue light irradiation (350 nm). The reaction mixture consisted of 100 µL of TMB (1mM), 200 µL of H_2O_2 (30% v/v), and 1.8 mL of sodium acetate buffer (NaAc, pH 4.5).

To evaluate singlet oxygen species ($^1O_2$), the system (CDs+TMB) was irradiated t at 350 nm for 30 minutes, after which 10 µL of sodium azide (NaN_3) was added to evaluate its effect as a $^1O_2$ scavenger. The absorbance at 652 nm was recorded using a UV-Vis spectrophotometer. Additionally, the absorbance measurements at 630 nm were taken every 5 seconds under 350 nm irradiation to monitor reaction kinetics. The decrease in absorbance upon NaN_3 addition was used to confirm the presence of $^1O_2$ as the primary reactive oxygen species responsible for the oxidation of TMB.

Photothermal Studies

Thermal studies were carried out by irradiating, in deionized water (control), CDs1, CDs2, CDs3 and CDs4 ($0.5\ mg{\cdot}mL^{-1}$), with red (630 nm) light and blue (450 nm) light and 30 $W.cm^2$ and taking the temperature every 2 minutes until it did not change.

Cell Culture

The cell cultures were maintained weekly using LLC-MK2 cells (strains of rhesus monkey kidney cells, source ATCC). They were maintained in Dubelco Modified Eagle Medium (DMEM) (Gibco), supplemented with 10% fetal bovine serum (Gibco), 1% penicillin/streptomycin (Gibco), and 1% pyruvate (Gibco) in T25 flasks (Thermo Scientific). Cells were passaged weekly, and a T25 flask was inoculated with 2×105 cells. The flasks were then incubated at 37 °C for 24 hours with relative humidity and supplemented with 5% CO_2. This process was performed to harvest the cells and conduct the necessary assays.

Cytotoxicity Assay

LLC-MK2 cells were harvested using trypsin and counted. In a 96-well plate, 2×104 cells were seeded per well from column 1 to column 11. The plate was then incubated for 24 hours at 37 °C with 5% CO_2 and relative humidity. On the following day, the plate was washed with 100 µL of PBS per well, and the 10 concentrations of CDs (4000, 2000, 1000, 500, 250, 125, 62.5, 31.2, 15.6, 7.8 $\mu g \cdot mL^{-1}$) were added from column 1 to column 10. Columns 11 and 12 were filled with 100 µL of culture medium and served as the cell viability and cytotoxicity control, respectively. Finally, 10 µL of Resazurin (3 mm) (Thermo Scientific) was added to each well, and the plate was incubated at 37 °C with 5% CO_2 for fluorescence reading at 24 hours and 8 days using the Glomax plate reader (Promega) with excitation wavelengths of 530–560 nm and an emission wavelength of 590 nm.

Antibacterial Activity

MRSA (ATCC: 700682) and *ESBL-producing E. coli* (ATCC: 43300), multidrug-resistant cryovials, were utilized as test organisms in antimicrobial investigation. Inoculating cryovials with Mueller–Hinton agar (Difco Laboratories) required thawing cryovials at room temperature. A 37 °C overnight incubation of the culture media was performed. After that, the concentration required for the bioassays was reached by diluting each medium according to its absorbance using Mueller–Hinton broth (Difco Laboratories), as assessed by spectrophotometry: For *ESBL-producing E. coli*, this is 107 $CFUs \cdot mL^{-1}$, while for *MRSA*, this is 106 $CFUs \cdot mL^{-1}$.

Upon reaching the indicated concentration, each medium was dispensed into microtubes: six aliquots of 1 mL per CDs (annatto, cinnamon, curcumin and hyper-concentrated sucrose at 2000 $\mu g \cdot mL^{-1}$) and six aliquots of 1 mL as control. Half of the aliquots were used to evaluate the activity of the nanocomposites under irradiation with blue light (450 nm; 40 $mW \cdot cm^{-2}$), while the other half was not exposed to these conditions.

For 10 minutes, the microtubes were centrifuged at 3000 rpm. To wash the cells and remove the remaining culture media, 1 mL of PBS was added after removing the supernatant. Under the same circumstances, the pellet was resuspended and recentrifuged. Each microtube was filled with 1 mL of the substance after discarding the PBS. The cells were once more resuspended in PBS in the control microtubes. Each tube was vortexed to dissolve the pellet once more before being incubated in the dark at 37 °C for 45 minutes.

Three aliquots of each substance and three controls were exposed to blue light at $40mW \cdot cm^{-2}$ after incubation. No radiation was applied to the remaining tubes.

Each aliquot was serially diluted in PBS. Each dilution was inoculated onto an 8-part Petri plate using a 4 µL aliquot and Mueller–Hinton agar. For colony isolation, each inoculum was streaked. Petri plates were incubated for 24 hours at 37 °C, and then the number of colonies in each dilution was counted.

Anticancer Activity

T47D cells (source, ATCC) were dispersed at the concentration indicated for bioassays of 2×105 cells per well with 10% DMEN. CDs3 was added to half of the samples at a concentration of 2000 $\mu g \cdot mL^{-1}$, and the other half of T47D cells with DMEN was used as control samples. All samples were incubated for 4 hours with 5% CO_2 and RH (relative humidity).

To evaluate the anticancer capacity of the CDs, one well from each group was taken from the control group and the group with CDs3 to be irradiated with red LED light (630 nm, 65.5 $mW \cdot cm^{-2}$) for 40 min (sample + red light), another to

be irradiated with blue LED light (450 nm; 40 $mW \cdot cm^{-2}$) for 30 min (sample + blue light), and another without irradiation (sample + dark).

Subsequently, the contents of each well were distributed in rows in a 96-well plate, and 10 µL of resazurin was to read the oxide-reduction of this compound and incubated in the same conditions. After 24 hours, the plate was read using the Glomax plate reader (Promega) with an excitation wavelength of 520 nm and an emission range of 580–640 nm. Therefore, the assays were duplicated in the 96-well plate and made on three days.

Results and Discussion

Shape, Size and Zeta Potential of the CDs

Based on the results acquired by TEM, it was possible to determine the shape and size below 10 nm of all the synthesized CDs.[1,2]

Figure 1A–D shows the corresponding TEM images of CDs1, CDs2, CDs3, and CDs4, respectively, identifying lattice spacings. CDs1 (see Figure 1A) presented an interplanar distance of 0.200 nm and 0.305 nm, corresponding to the (100) and (002) planes of graphite, respectively. These values are characteristic of CDs with a graphitic structure, suggesting the ultrafine crystallite size typical of carbon quantum dots (CQDs). However, the distance d = 0.231 nm has not been commonly reported in previous studies on CDs. It could be related to a less ordered structure or the presence of defects in the crystal lattice of the CDs. CDs2 (see Figure 1B) displayed an interplanar distance of 0.335 nm, which aligns with the (002) plane of the graphite plane. According to Nie et al,[76] this lattice is related to fluorescent CDs. Concerning CDs3 (see Figure 1C), the interplanar distances were 0.184 nm, 0.185 nm and 0.175 nm, corresponding to the (102) crystalline planes of graphite.[77] While CDs4 showed lattice distances of 0.367 nm, 0.355 nm and 0.348 nm, corresponding to the (002) crystalline planes of graphite (see Figure 1D).

The electron pattern of CDs2 is shown in Figure 1E. According to Diwan et al,[78] the broad diffused ring in the Selected Area Electron Diffraction (SAED) pattern reveals that a significant body of the synthesized CDs is amorphous. Nevertheless, well-defined crystalline CDs are detected in the indexed ring pattern shown in Figure 1E. The inter-layer d-spacing is 0.36 nm, corresponding to (002), and the 0.23 nm inter-layer d-spacing to plane (100) of graphite.[78]

The particle sizes of CDs exhibited an overall mean diameter of 2.82 nm, with a global standard deviation (SD) of 0.61 nm, indicating moderate variability in size. Each type of CDs displayed distinct mean sizes: CDs1 had an average size of 2.867 nm (SD = 0.673), CDs2 had a mean size of 2.428 nm (SD = 1.057) (see Figure 1F), CDs3 measured 2.336 nm (SD = 0.701), and CDs4 presented the largest average size at 3.665 nm (SD = 1.114). The distribution of particle sizes was somewhat heterogeneous, as evidenced by kurtosis values, suggesting a spread that includes smaller and larger particles relative to the mean. Specifically, CDs1 exhibited a positive kurtosis (1.044), indicating a slightly peaked distribution, while CDs2, CDs3, and CDs4 displayed negative kurtosis values (−0.805, −1.259, and −0.577, respectively), suggesting a broader distribution. The minimum and maximum sizes observed were 0.278 nm (CDs2) and 6.017 nm (CDs4), respectively. The median particle sizes were close to the mean for each sample, further supporting a relatively symmetric distribution. These results are in agreement with the data previously reported in literature.[1,2]

The histogram (see Figure 1G) revealed that the particle size distribution of CDs generally follows a normal distribution; however, some atypical measurements, particularly larger particles up to 5 nm or more, were noted beyond the typical range. Table 1 summarizes these results, including the global mean particle size of 2.824 nm and the global SD of 0.61 nm, along with specific metrics (standard deviation, kurtosis, minimum, median, and maximum) for each type of CDs. This study found that the synthesized CDs had irregular shapes, probably due to an uncontrollable synthesis process.[79] Besides, using the microwave-assisted technique makes it difficult to have monodispersed nanoparticles. The aggregation of CDs in this process is inevitable since the raw liquid was dried entirely in the microwave oven.[79] For instance, Vasimalai et al synthesized CDs from cinnamon with sizes of 3.5 ± 0.1 nm,[80] which, compared with our results, seems smaller. Nevertheless, the effect of agglomeration also must be considered.

By DLS were measured the hydrodynamic diameters of the CDs on different days. The results are presented in Table 2. Consider that the sizes measured by DLS correspond to a mean hydrated diameter assuming spherical particles. This technique makes it impossible to distinguish if the measured value corresponds to an agglomerate or single particle

Table 1 Descriptive Statistics of the Particle Size Distribution of CDs

CDs	N total	Mean	Standard Deviation (SD)	Sum	Kurtosis	Minimum	Median	Maximum
CDs1	53	2.86723	0.67365	151.963	1.04417	1.746	2.831	5.015
CDs2	32	2.42809	1.05714	77.699	−0.80551	0.278	2.695	3.704
CDs3	28	2.33575	0.70124	65.401	−1.25979	1.131	2.449	3.553
CDs4	34	3.66474	1.11423	124.601	−0.57725	1.974	3.3555	6.017
Global mean	2.82395							
Global SD	0.60549							

Table 2 CDs Hydrodynamic Diameters After a week

Sample	Size at day 0 (nm)	Size at day 7 (nm)	ZP (mV)
CDs1	25	35	−28.5±1.4
CDs2	83	23	−29.4±1.3
CDs3	75	24	−29.0±1.4
CDs4	200	91	−21.0±1.7

since an average is calculated.[81] These results could be a consequence of three factors: (i) agglomeration degree, (ii) attached molecules in the CDs, and/or (iii) the presence of bigger organic by-products.[81] In any case, considering the data of day 7, the size of the CDs agglomerates was established as CDs4>CDs1>CDs3>CDs2. The CD hydrodynamic diameters in Table 2 also indicate a tendency to disaggregate from day 0 to day 7. This shows that on day 7, hydrodynamic diameters had a lower value in relation to day 0, except for CDs1.

Regarding Zeta potential (ZP) results, they are also shown in Table 2. The values of CDs1, CDs2, and CDs3 were close to −30 mV, and according to Sahiner et al[82,83] and Hua et al[82,83] this indicates that CDs possess good stability owing to the interparticle electrostatic repulsion.[84] Thus, the negative charge is sufficient for CDs1, CDs2, and CDs3 to form stable colloidal dispersions at neutral pH. Considering the absolute values of Table 2, the CDs4 presented the lowest ZP, which is coherent with Figure 1 since the CDs4 had the most considerable particle size.

Chemical Composition of the Synthesized CDs

Figure 2a presents the FTIR spectra of CDs1, CDs2, CDs3, and CDs4. Remember that the intermediate species (species that were formed during the synthesis but disappeared during the process), which form the CDs in each mechanism through diverse pathways, are different and directly dependent on the chemical nature of the precursor.[85,86] However, some common functional groups were identified, especially in the 2000–800 cm^{-1} wavenumber range fingerprint region.

In the zones marked with red, between ~3550-2900 cm^{-1}, are situated broad and intense bands of the functional groups O-H and N-H (stretching vibration). The first one might indicate the presence of hydroxyl moieties.[87–89] Only in CDs3 was distinguished the C=O group, in ~1725 cm^{-1} highlighted in blue, denoting the existence of carboxyl groups.[90] In all CDs were identified C=C bonds, marked in green, they are situated at ~1650–1600 cm^{-1}. This band possibly corresponds to the benzene ring of the CDs.[91,92] Besides, C-N bonds were identified, pointed in sky-blue, which should demonstrate amine groups in CDs1, CDs2, and CDs4.[93] In all samples detected, C-H and C-O functionalization, marked with orange (~1500–1450 cm^{-1}) and purple (~1250–1125 cm^{-1}), correspondingly.[94] Moieties such as hydroxyls, amines, and carboxyl groups contribute to the water dispersibility of the CDs due to these functionalization's attributes of hydrophilic nature.[95–97] This functionalization, along with the strong negative charge, could be related to the antimicrobial and antitumoral capacities of the CDs.[82]

Raman spectroscopy results of the CDs are depicted in Figure 2b, where it is easy to distinguish the characteristic bands of the carbon-based materials, reported elsewhere.[98,99] D-band (defect or disorder at ~1350 cm^{-1}) and G-band

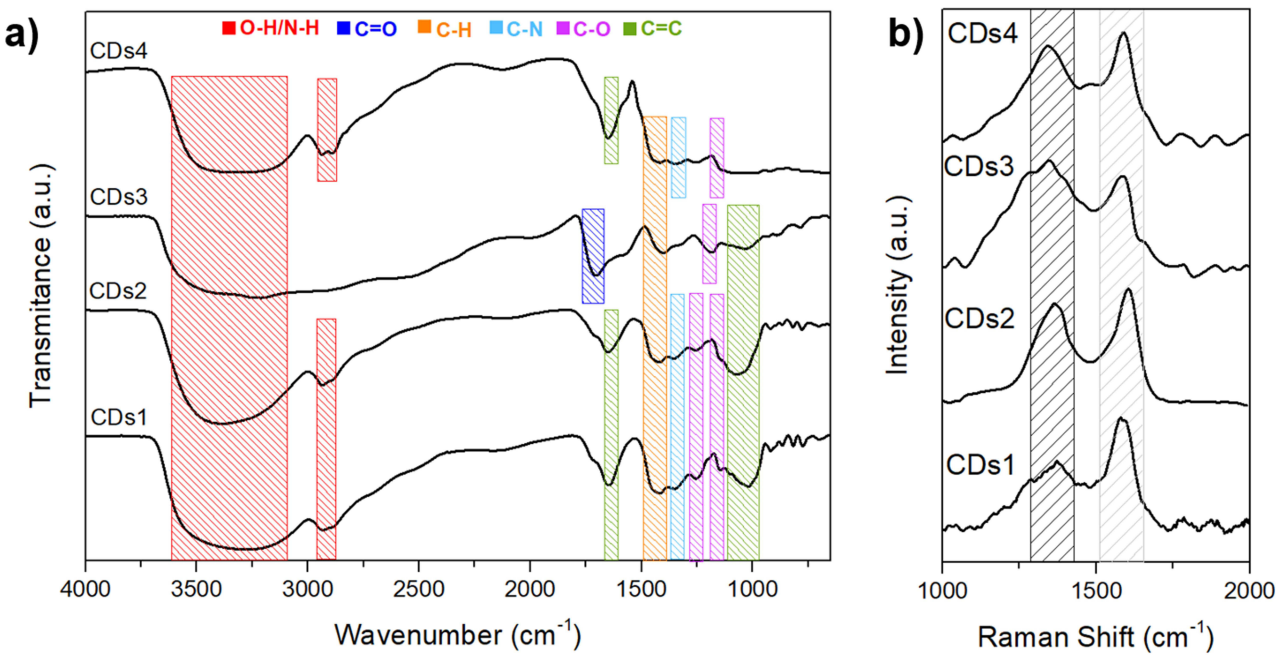

Figure 2 (**a**) FTIR and (**b**) Raman spectra of the synthesized CDs.

(graphite at ~1580 cm^{-1}), marked in black and grey, correspondingly.[98,99] The D-band corresponds to sp^3 hybridized carbon atoms and the presence of structural defects, while the G-band is related to sp^2 hybridized carbon atoms associated with well-organized carbon.[100] Only in CDs3 the intensity of the D-band is slightly higher than that of the G-band, indicating that these CDs have some defects sp^2 carbons. The rest of the CDs presented a superior G-band than D-band. The relative intensity ratio of D-band to G-band, as ID/IG, measures the extent of disorder or a degree of graphitization.[101] The Raman result of CDs1 (lowest ID/IG value, low degree of graphitization of all CDs) agrees with the interplanar distance of CDs1, which does not indicate the presence of graphitic material that could confirm the presence of defects in the crystalline structure (TEM analysis). These defects could produce greater dispersion of the CDs, showing this in the smallest hydrodynamic size of all the CDs (DLS analysis after 7 days later). Conversely, the higher degree of graphitization corresponds to CDs3, which means that this sample has the most "ordered structure" since graphitization is the degree of rearranging carbon atoms to fill atom vacancies and improve atom layout. Consequently, if the crystalline structure changes, it has antibacterial and antitumoral features.[102]

Luminescence of CDs

The photoluminescence emission spectrum obtained from 400 to 700 nm of all the CDs are depicted in Figure 3 (A: CDs1, B: CDs2, C: CDs3 and D: CDs4). The CDs showed strong and stable photoluminescence dependent on the excitation wavelength. The longer the excitation wavelength, the more emission bands of longer wavelength are observed, but with lower intensity. The highest intensity was detected at an excitation wavelength of around 420 nm, with emission at around 530 nm for all CDs. It was also confirmed that at an excitation wavelength of 600 nm, there is still a band with a low emission intensity of around 650 nm. This data shows that all CDs presented the highest luminescence in the visible region of the spectrum. The divergent peak position, spectral width, and shape might be related to factor such as size, surface state, and/or sp^2-sp^2-hybridized carbon domains (located in the carbon core).[103–105] The highest emission was detected at ~530 nm in all the cases.

These results can motivate future studies since they encourage the application of CDs as antibacterial agents by exciting with blue light of around 400 nm (see Figure 4), which is related to soft light penetration into the skin, as well as tumor elimination at 600 nm that results in greater light penetration into the skin.[106,107]

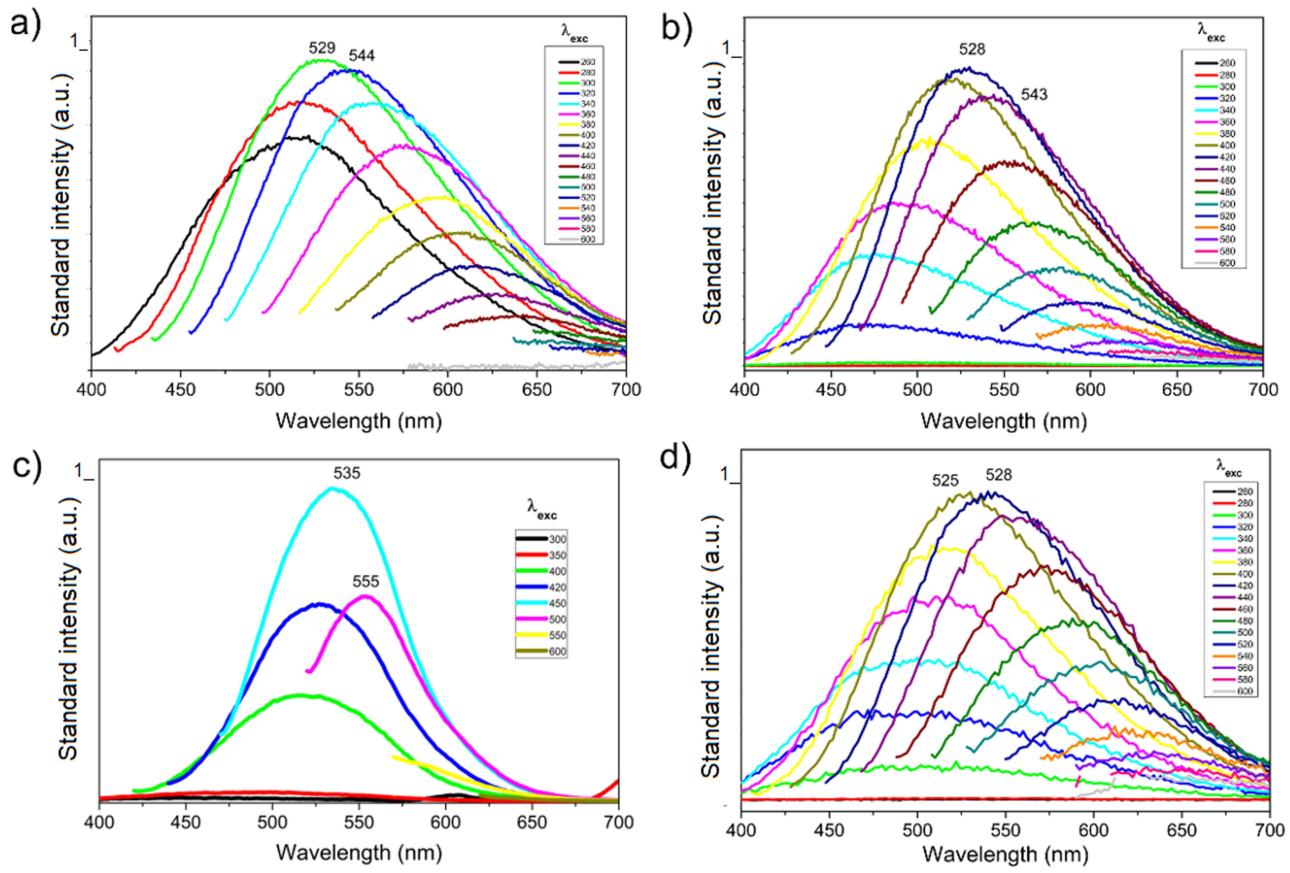

Figure 3 Emission spectrum of the synthesized CDs. (**a**) CDs1, (**b**) CDs2, (**c**) CDs3 and (**d**) CDs4.

Photodynamic Analysis of CDs

The photodynamic activity of CDs was evaluated based on the oxidation of 3,3′,5,5′-tetramethylbenzidine (TMB). The oxidation process leads to the formation of oxidized TMB (oxTMB), which is characterized by an increase in absorbance over time. Figure 5 illustrates the absorbance difference at 652 nm between the TMB/H_2O_2 + CDs system and the control (TMB/H_2O_2) under light irradiation (A_{Light}) and dark conditions (A_{DC}) as a function of time. Each bar represents the standard deviation (0.0029) based on triplicate measurements.

Each CDs sample exhibited a distinct oxidation rate, with saturation times as follows: CDs1 at 120s, CDs2 at 55s, CDs3 at 160s, and CDs4 at 50s. Among all samples, CDs3 demonstrated the highest absorbance, followed by CDs1, CDs2, and then CDs4. The negligible absorbance observed in the TMB/H_2O_2 control confirms that the CDs play a crucial catalytic role in the process of oxidation under light irradiation. This steady increase in absorbance over time, particularly under blue light irradiation at 450 nm, highlights the ability of each CD samples to generate ROS which catalyze the oxidation of TMB to oxTMB.[108]

To confirm the involvement of singlet oxygen ($^1O_2$) in the oxidation of TMB, sodium azide (NaN_3) was introduced as a selective scavenger. This experiment was performed by irradiating each sample under blue light irradiation at 450 nm for 30 minutes, followed by the addition of 10 µL of NaN_3. The results, described in Figure 6, show a significant reduction in absorbance at 652 nm upon the introduction of NaN_3, confirming the presence of $^1O_2$ as the primary ROS responsible for the oxidation process. NaN_3 is a well-established quencher of $^1O_2$ due to its rapid reaction through both physical and chemical deactivation mechanisms. The primary pathway involves converting $^1O_2$ into a less reactive species via the formation of azide radicals (N_3^-). Wu et al reported that this reaction effectively suppresses TMB oxidation by depleting $^1O_2$, resulting in a decreased absorbance at 652 nm. Since $^1O_2$ is crucial for initiating TMB oxidation, the significant reduction in oxTMB formation upon NaN_3 addition further confirms the predominant role of

https://doi.org/10.2147/IJN.S507574

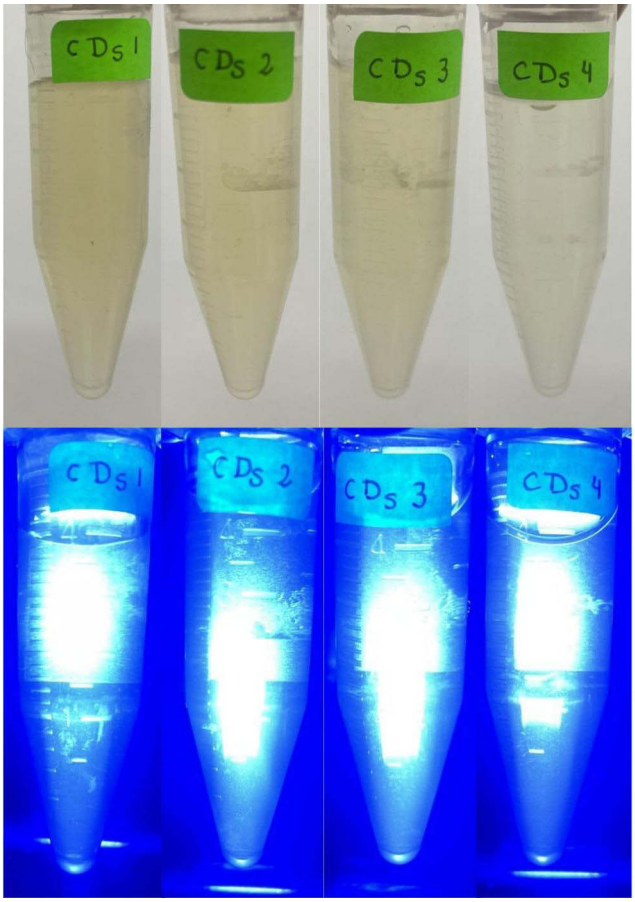

Figure 4 Photographs of CDs under day light and blue light.

$^1O_2$ in the photodynamic activity of the CDs.[108] The most pronounced decrease in absorbance was observed for CDs3, indicating its superior $^1O_2$ generation capability. This suggests that the structural and chemical properties of CDs3, synthesized from curcumin, enhance its photodynamic performance. According to Najaflu et al, the presence of π-π interactions within the benzene ring contributes to the enhanced photodynamic activity of CDs.[109] Similarly, CDs2 and CDs1 also exhibited notable reductions in absorbance, indicating substantial $^1O_2$ production under blue light irradiation. In contrast, CDs4 showed the least reduction, suggesting lower photodynamic activity compared to the other CDs. This reduced efficiency may be attributed to the chemical composition of sucrose-derived CDs, which lack aromatic structures that facilitate efficient ROS generation.[110]

The average size of the CDs was equally determined to be 2.82 nm as reflected in Table 1. This gives a huge specific area of surface, which is critical for superb catalytic activity. Moreover, the presence of benzene rings of CDs allows the interaction with biphenyl of TMB molecules by means of some π-π stacking, promotes the favorable vicinity for the surface of the substrate and hence improves the catalytic function.[111,112] Also, the high contents of carbon within the CDs indicate that the carbon nuclei that developed were well formed and stable for optimal reactivity and stability needs.[111] Previous research also highlights that the efficiency of photodynamic activity in CDs is enhanced by factors such as particle size, surface functionalization, and the presence of conjugated systems (eg benzene rings).[111–113] The small size of the CDs and their high surface area-to-volume ratio provide wide active sites for the catalytic reaction, making them competitive with other nanocatalysts.

Photothermal Analysis

The heating profiles of CDs1, CDs2, CDs3, and CDs4 were compared to deionized water as a control (see Figure 7). The results demonstrated that CDs1, CDs2, and CDs3 exhibited higher temperature increases under both irradiation

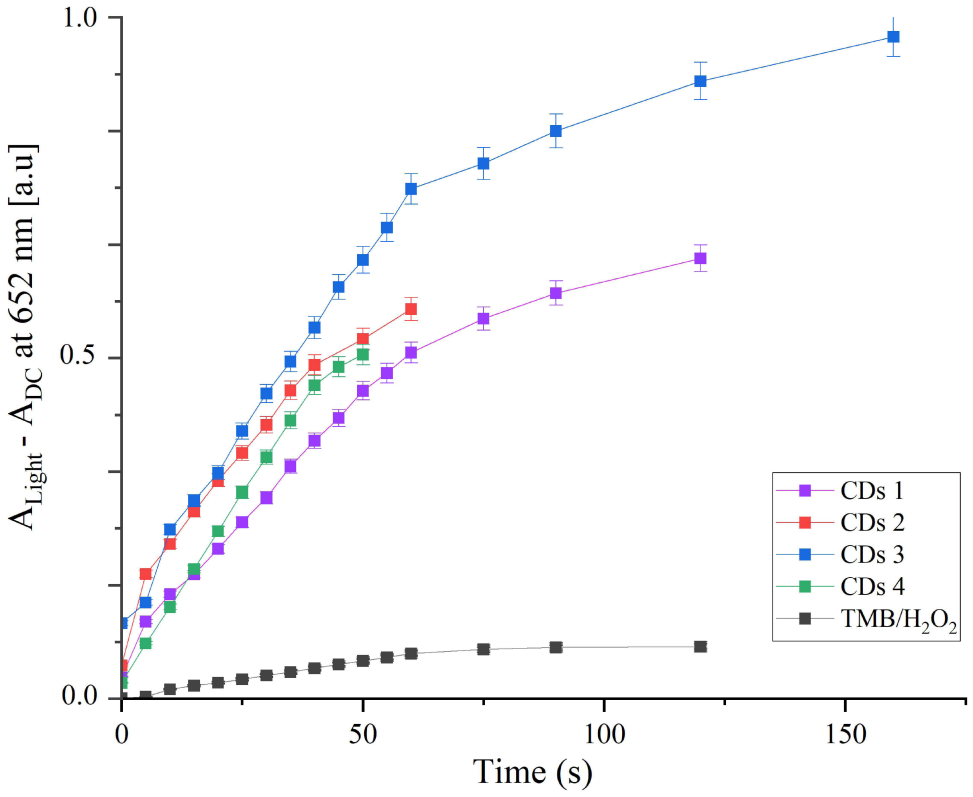

Figure 5 POD-like activity of CDs under light irradiation: Difference of absorbance vs Time.

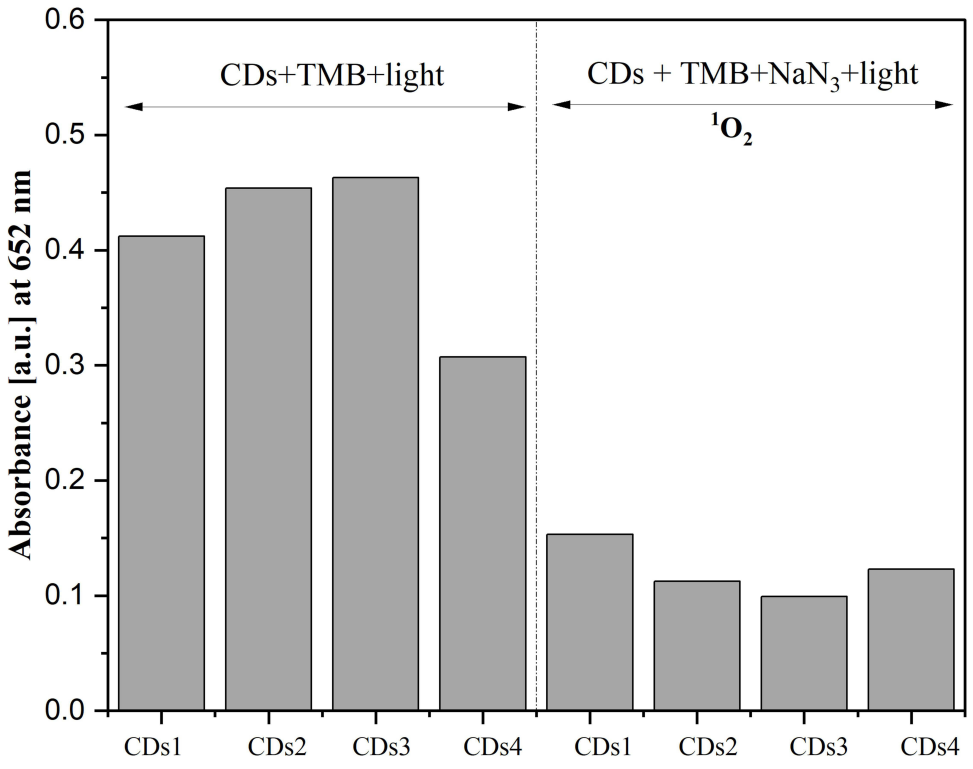

Figure 6 Irradiation of CDs1, CDs2, CDs3 and CDs4 under blue light (450 nm) for 30 minutes and addition of NaN_3.

https://doi.org/10.2147/IJN.S507574

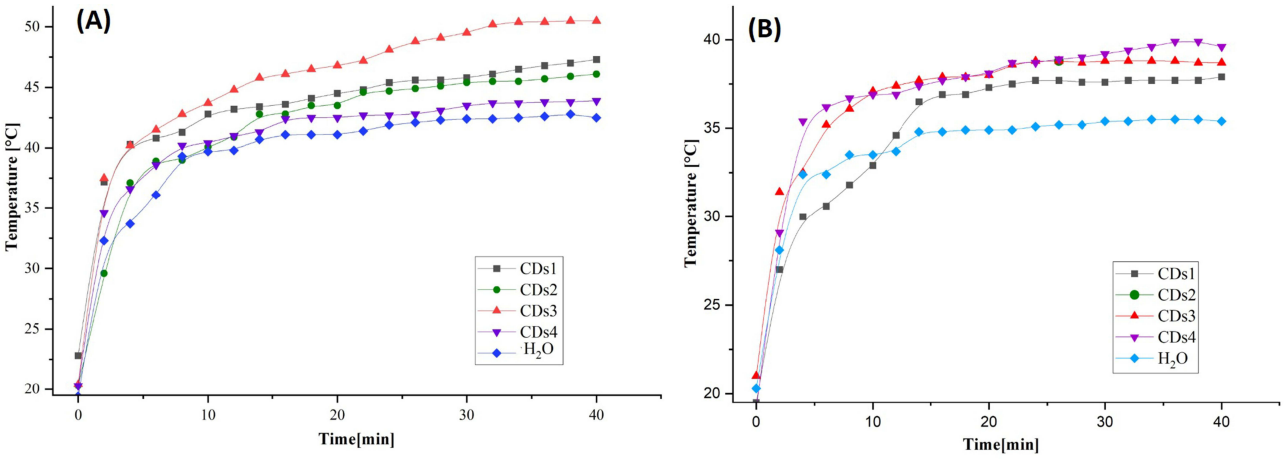

Figure 7 Heating profiles of CDs1, CDs2, CDs3, and CDs4 at (**A**) Blue light and (**B**) Red light.

conditions, indicating strong photothermal conversion properties. In contrast, CDs4 showed a limited rise in temperature, suggesting weaker photothermal activity.

Under blue light irradiation (450nm), CDs1, CDs2, and CDs3 reached temperatures of approximately 50 °C (see Figure 7A), whereas CDs4 only increased to ~30–35°C. The control exhibited minimal temperature changes, confirming that the observed heating was due to the photothermal properties of the CDs. Red light irradiation (630 nm), which is more relevant for biomedical applications due to its deeper tissue penetration,[114] resulted in maximum temperatures around 40 °C for CDs1, CDs2, and CDs3, while CDs4 displayed only an increase, not exceeding 30°C (see Figure 7B). Sun et al investigated CDs synthesized from different organic precursors and found that those with π-π conjugated structures exhibited superior photothermal properties. This supports our hypothesis that CDs1, CDs2, and CDs3 possess structural features favorable for photothermal conversion, while CDs4 may lack these key characteristics.[114] These results suggest that CDs1, CDs2, and CDs3 possess effective photothermal conversion capabilities, making them promising candidates as photothermal agents for PTT applications.

Cytotoxicity Analysis in LLC-MK2 Cells

The percentage of cell viability of monkey kidney cells (LLC-MK2), at concentrations up to 4000 $\mu g \cdot mL^{-1}$ (LOG concentration = 3.60) of all CDs, did not present significant changes at 24 h and 48 h (see Figure 8a and b). The cell viability of LLC-MK2 cells at concentrations of up to 4000 $\mu g \cdot mL^{-1}$ of CDs2, CDs3, and CDs4 did not present significant changes (80–100%) at 24 h, as well as concentrations of up to 2490 $\mu g \cdot mL^{-1}$ of CDs1. In contrast, after 48 h, the CDs1, CDs2, CDs3, and CDs4 samples did not show significant differences in cell viability (80–100%) for concentrations up to 2000 $\mu g \cdot mL^{-1}$. This result is consistent with studies at high concentrations of CDs (1000–4000 $\mu g \cdot mL^{-1}$), where negligible cytotoxicity is reported.

The IC_{50} corresponding to 50% cellular inhibition caused by the presence of CDs2, CDs3, and CDs4 were calculated in OriginLab software with a 95% confidence interval with a sigmoidal fit Dose-Response. This information is detailed in Table 3. It is worth noting that the IC_{50} values obtained are not within the concentration range used in this assay. Within the results obtained, it can be observed that the IC_{50} of CDs3 doubles the other CDs, which agrees with the literature since CDs based on curcumin have been shown to have high biocompatibility with normal cells and almost no cytotoxicity at high concentrations (10 μM).[66]

The robust catalytic activity observed in the POD-like studies, especially for CDs3, suggests enhanced oxidative stability and high surface reactivity, likely responsible for its biocompatibility. The structural stability and lower cytotoxicity of CDs3 can be advantageous, as higher biocompatibility permits application in biological systems at significant concentrations without adverse cellular effects. This property further aligns with findings that curcumin-

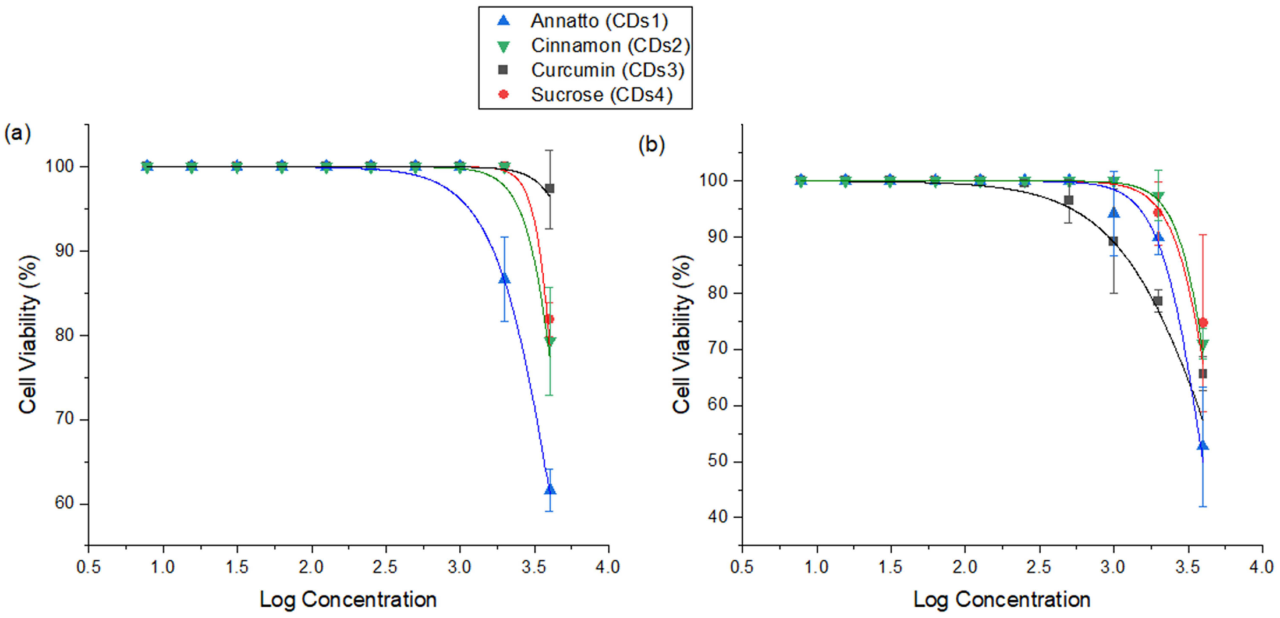

Figure 8 Cell viability percentage in monkey kidney cells by Resazurin cell viability assay, using CDs1, CDs2, CDs3, and CDs4, at concentrations between 7.81–4000 $\mu g \cdot mL^{-1}$ for (**a**) 24 h and (**b**) 48 h. Data represent the mean ± SD (n= 3 per group).

based CDs show high biocompatibility, supporting their suitability in therapeutic applications without substantial toxicity.[110,115]

Antibacterial Studies

The antimicrobial effect of the CDs was evaluated against the microorganism's *methicillin-resistant S. aureus* (*MRSA*) and *Extended-Spectrum β-Lactamase (ESBL)-producing E. coli*, using a CDs concentration of 2000 $\mu g \cdot mL^{-1}$, and blue light irradiation (450 nm) at 40 mW cm^{-2} for 30 min.

The results obtained for each colony are shown in Figure 9. The histograms present the LOG ($CFUs \cdot mL^{-1}$) evaluation standardized to 1. The established concentration for bioassays was used, which is 107 $CFUs \cdot mL^{-1}$ for *MRSA* and 106 $CFUs \cdot mL^{-1}$ for *ESBL-producing E. coli*. These results show that light alone cannot eliminate microorganisms (control + light samples); to combat the microorganisms, it was necessary to irradiate the samples in the presence of CDs (CDs1+ light, CDs2 + light, CDs3+ light, and CDs4+ light).

Figure 9 presents the quantitative result of the colony counts of (A) *MRSA* and (B) *ESBL-producing E. coli*., before and after being irradiated with blue LED light (450 nm, 40 $mW \cdot cm^{-2}$). This figure indicates that the colonies of *MRSA* and *ESBL-producing E. coli* (samples CDs1+ dark, CDs2+ dark, CDs3+ dark, and CDs4+dark) were not different from the control group. In contrast, the bacteria colony count in samples CDs1 + light, CDs2 + light, CDs3+ light, and CDs4 + light was significantly lower than the control group (*** $p \leq 0.001$) for *ESBL-producing E. coli* and CDs1 + light, CDs2 + light, and CDs3 + light, was significantly lower than the control group (*** $p \leq 0.001$) for *MRSA*. This means that after irradiation, CDs1, CDs2, and CDs3 eliminated all *MRSA* and *ESBL-producing E. coli*, and CDs4 can only completely

Table 3 IC50 of CDs at 24 h and 48 h

Sample	IC_{50} at 24 h ($\mu g \cdot mL^{-1}$)	IC_{50} at 48 h ($\mu g \cdot mL^{-1}$)
CDs1	5011.9	3981.0
CDs2	5623.4	3981.0
CDs3	10000.0	5011.9
CDs4	5011.9	5011.9

https://doi.org/10.2147/IJN.S507574

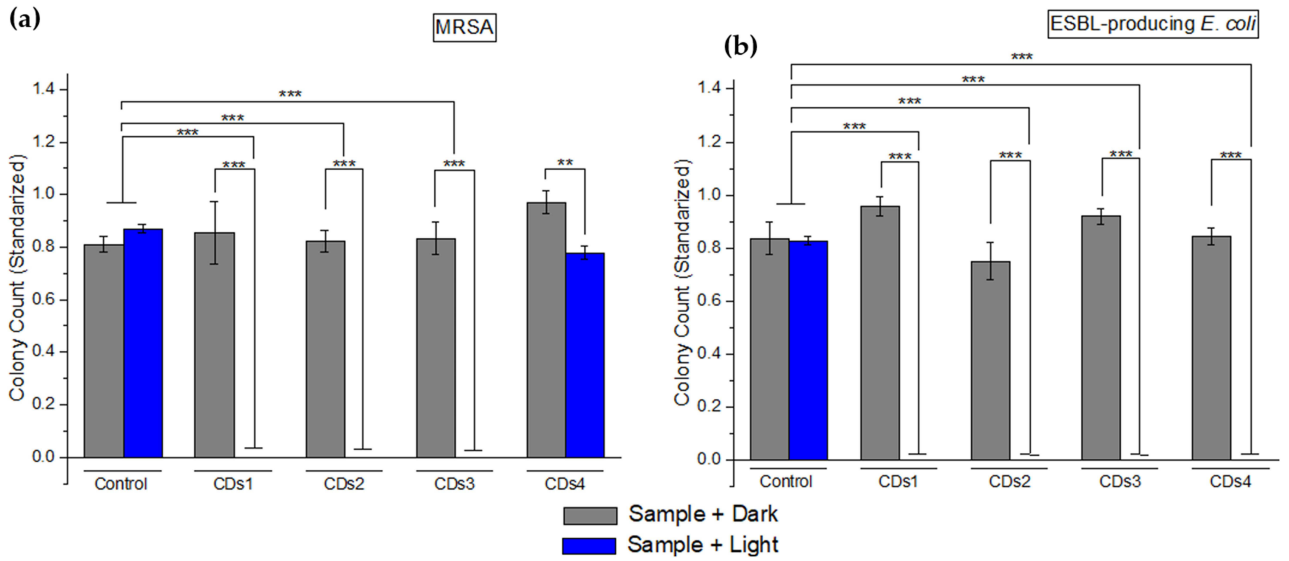

Figure 9 PDT/PTT antimicrobial effect. Standardized result of LOG (UFC/mL) by (**a**) *MRSA* and (**b**) *ESBL-producing E. coli*, based on CDs1, CDs2, CDs3 and CDs4. The concentration of CDs was 2000 μg·mL^{-1}. Time of irradiation of CDs was 30 min. Significant differences in means according to the Tukey's test (**p ≤ 0.01, and *** p ≤ 0.001).

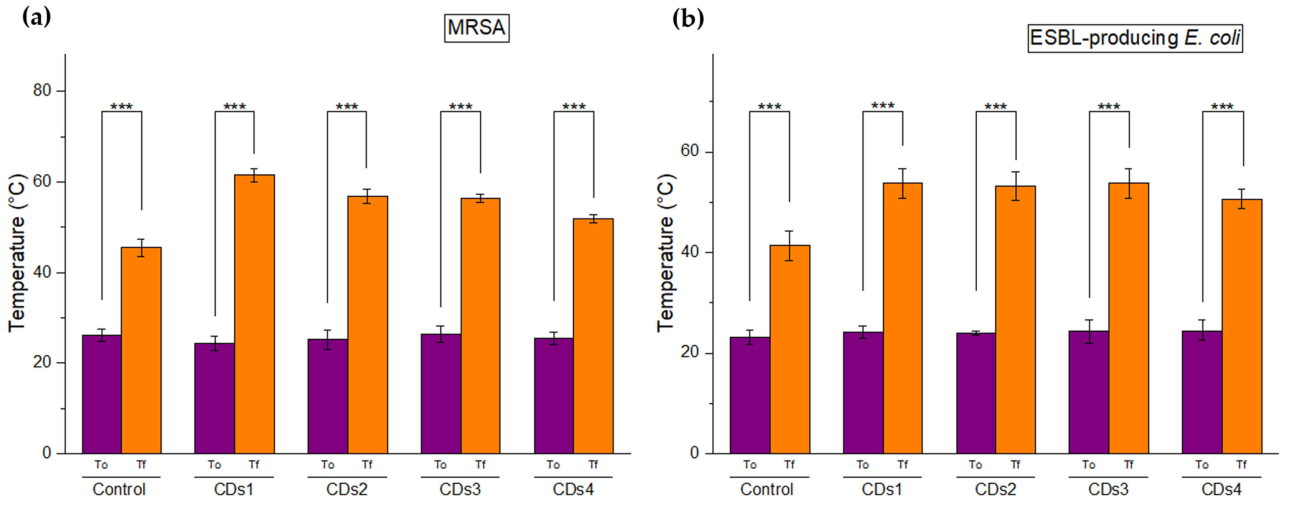

Figure 10 Sample temperatures of (**a**) *MRSA* and (**b**) *ESBL-producing E. coli*, based on CDs1, CDs2, CDs3, and CDs4 before (To) and after (Tf) being irradiated with blue light. The concentration of CDs was 2000 μg·mL^{-1}. Time of irradiation of CDs was 30 min. Significant differences in means according to the Tukey's test (***p ≤ 0.001).

remove *ESBL-producing E. coli*. Therefore, all CDs can eliminate some of the microorganisms used in this study, with CDs1, CDs2, and CDs3 being the best due to their ability to eliminate the two types of bacteria. According to Figure 10, the elimination occurs by bimodal strategy PDT/PTT, where it is observed that the temperature after irradiation rises to around 50 °C evidencing the PTT effect, and from the literature, it is known that CDs can act as PS-based PDT effect.[116,117] Yan et al, Romero et al, and Lin et al showed that the rise in temperature changes bacterial outer membrane permeability through PTT, significantly weakening bacterial activity, promoting PDT singlet oxygen diffusion into cells, disrupting the homeostatic state of cells, and synergistically enhancing the antibacterial effect.[66,118,119]

CDs can generate ROS, such as singlet oxygen, which is highly reactive and can induce microbial cell death by necrosis/apoptosis.[120] The ROS causes oxidative damage to various cellular components, including proteins, nucleic acids, and lipids, leading to the destruction of microorganisms.[120,121]

The antimicrobial activity of the CDs used in this research based on the PDT/PTT strategy exhibits a 100% inhibition of *ESBL-producing E. coli* in comparison with other types of CDs without using phototherapy such as CDs coated $CaCO_3$ nanocarrier conjugated with levofloxacin (CDs-CCNC- Lvx) obtained in the study by Kanwal et al where inhibition of 68% is achieved.[122] In addition, CDs1, CDs2, and CDs3 eliminate *MRSA* by applying the PDT/PTT strategy using a red light for 30 min, which, in comparison to the study without phototherapy by Kung et al, presents an improvement in treatment time and concentration of CDs, since this study shows elimination of *MRSA* after 24 hours of application of citric acid CDs at a concentration of 2500 $\mu g \cdot mL^{-1}$.[122]

ESBL-producing E. coli are classified as Gram-negative bacteria and have a relatively thinner peptidoglycan layer in their cell walls, making them more vulnerable to heat and ROS,[123] allowing the CDs studied to eliminate this type of colony. *MRSA* strains are classified as Gram-positive bacteria and have a thicker peptidoglycan layer in their cell wall, which provides some protection against heat.[124] In this case, CDs1, CDs2, and CDs3 present antimicrobial molecules that effectively eliminate *MRSA* in addition to the PDT/PTT effect. CDs4, being made up mainly of sucrose, does not demonstrate antibacterial properties, which agrees with the literature where it has been shown that high concentrations of sucrose do not cause microbial inhibition.[125]

The photothermal performance of the CDs was further correlated with their antimicrobial activity. The ability of CDs1, CDs2, and CDs3 to generate significant heat under irradiation aligns with their complete elimination of *MRSA* and ESBL - *Escherichia coli*. In contrast, CDs4, which displayed a weaker photothermal response, was only effective against ESBL-producing *E. coli* but failed to eliminate MRSA.

The antimicrobial activity of the synthesized CDs was evaluated in correlation with their PDT efficacy. The mechanism of microbial elimination involves the generation of ROS, particularly $^1O_2$, which induces oxidative stress, leading to cell membrane damage and microbial death. CDs3, derived from *Curcuma longa L*., exhibited the highest $^1O_2$ generation, as evidenced by its superior oxidation rate and significant reduction of absorbance at 652 nm with the presence of NaN_3. This enhanced ROS generation directly correlated with its antimicrobial efficacy, leading to the complete elimination of *MRSA* and *ESBL-producing Escherichia coli*. The effectiveness of CDs3 against these pathogens suggests that its structural properties, including the presence of conjugated benzene rings, facilitate efficient ROS-mediated bacterial inactivation. Similarly, CDs1 and CDs2 demonstrated substantial ROS production and notable antimicrobial activity, whereas CDs4 showed the weakest photodynamic response and lower microbial inhibition, likely due to its lack of aromatic structures that enhance ROS generation. CDs3, in particular, demonstrated the most favorable combination of high photothermal conversion, ROS generation, and biological efficacy, making it an excellent candidate for further investigation in photothermal and photodynamic therapy applications.[118]

The photothermal performance of the synthesized CDs was directly correlated with their antimicrobial efficacy. CDs1, CDs2, and CDs3 exhibited significant heat generation under irradiation, leading to the complete elimination of MRSA and ESBL-producing *Escherichia coli*. In contrast, CDs4, which demonstrated a weaker photothermal response, effectively inhibited ESBL-producing *E. coli* but failed to eradicate MRSA. This trend aligns with findings from previous studies by Bhavikatti et al and Wang et al, where CDs synthesized from ginger and garlic demonstrated high photothermal conversion efficiency, achieving superior antibacterial effects (90%) through localized hyperthermia-induced membrane disruption. This enhanced antibacterial activity is attributed to the intrinsic properties of the carbon source, which influence the structural and electronic characteristics of the CDs, thereby optimizing their photothermal and antimicrobial performance.[126,127]

Furthermore, the antimicrobial activity of the CDs was closely associated with their photodynamic efficiency. The primary mechanism of microbial inactivation involved the generation of ROS, particularly $^1O_2$, which induced oxidative stress and membrane damage, ultimately leading to bacterial cell death. CDs3, synthesized from *Curcuma longa L*., exhibited the highest $^1O_2$ generation, as demonstrated by its superior oxidation rate and significant reduction in absorbance at 652 nm upon the addition of NaN_3. This result is consistent with previous research by Yan et al, who synthesized CDs from the turmeric plant as a carbon source and demonstrated that CDs with high aromatic content and conjugated π-systems facilitate efficient ROS production, thereby enhancing PDT efficacy against bacterial pathogens.[112,113]

Similarly, CDs1 and CDs2 displayed substantial ROS production and antimicrobial activity, reinforcing the role of PDT in microbial elimination. In contrast, CDs4 exhibited the weakest photodynamic response, which correlated with its lower antibacterial activity. This diminished effect may be attributed to its structural composition, as CDs lacking aromatic systems tend to generate ROS less efficiently, limiting their photodynamic potential.[113] Overall, CDs3 demonstrated the most favorable combination of high photothermal conversion, robust ROS generation, and potent antimicrobial efficacy, positioning it as a promising candidate for further applications in photothermal and photodynamic antimicrobial therapies.

Antitumoral Studies

The compounds CDs1, CDs2, CDs3 and CDs4 have similar characteristics. This was observed in the chemical, morphological, photophysical and bacterial elimination analysis using the CDs' synchronous PDT/PTT strategy. In this way, for antitumor studies of kidney CDs in T-47D cells (human breast cancer cell line) the compound CDs3 was chosen. In addition, the compound CDs3 shows the highest IC_{50} according to the cytotoxicity studies of monkey cells (LLC-MK2), which indicates that it is the least cytotoxic of all CDs.

The results obtained are shown in Figure 11. The histograms present the percentage of cell viability. A concentration of 2×105 cells per well-established bioassays was used. These results show that light alone does not have anticancer effects, which can be observed in the control bars, which indicates that to eliminate cancer cells, it is necessary to irradiate the samples in the presence of CDs3.

Furthermore, a significant difference was observed between cells irradiated with red and blue light, with lower cell viability (greater cell death) in the presence of CDs3 and red light. This result is consistent with previous research by Tiron et al, where carbon dots derived from herbal medicine demonstrated enhanced photodynamic efficacy against breast cancer cells, resulting in cell viability below 10% under red light irradiation. This effect is attributed to the superior absorption of red light by the CDs, which enhances ROS generation—particularly singlet oxygen ($^1O_2$)-leading to increased oxidative stress and apoptosis in cancer cells. The extended penetration depth of red light also allows for more effective activation of CDs in deeper tissue layers, further enhancing their photodynamic therapeutic potential.[128,129]

The photodynamic and photothermal properties of the CDs were investigated for their potential in antitumoral applications. PDT relies on the generation of ROS, primarily $^1O_2$, to induce oxidative stress, leading to apoptosis or

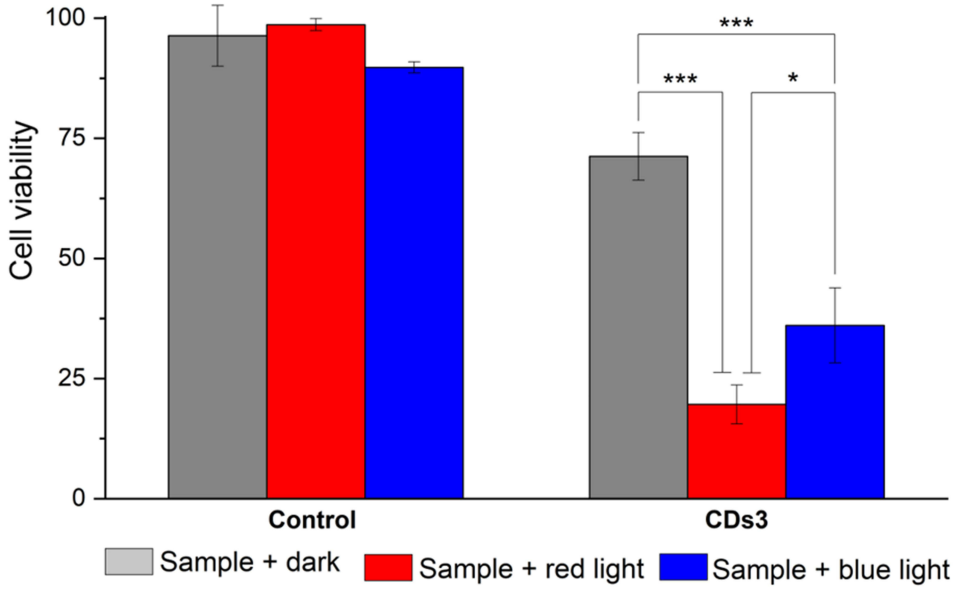

Figure 11 PDT/PTT anticancer effect. Samples Control (T47D cells+DMEN) and Samples with CDs3. The concentration of CDs3 was 2000 μg·mL^{-1}. Time of irradiation of CDs was 40 min with red LED light and 30 min with blue LED light. Significant differences in means according to the Tukey's test (*p ≤ 0.05 and *** p ≤ 0.001).

necrosis in cancer cells. Under red light irradiation (630 nm), CDs3 demonstrated remarkable Photothermal conversion, reaching temperatures of approximately 40 °C—a range known to induce hyperthermia-mediated cancer cell death. This finding is consistent with the studies conducted by Geng et al, Kim et al, and Najaflu et al, which demonstrated the effectiveness of CDs synthesized from biomass in photothermal cancer therapy under low-power red light irradiation. Their conclusions indicated that increasing the temperature to approximately 50 °C led to efficient tumor elimination through a synergistic photothermal effect, triggering irreversible protein denaturation and cell membrane disruption.[109,130,131] Likewise, the dual PDT-PTT effect observed in CDs3 highlights its strong potential for tumor ablation, where ROS-mediated oxidative stress works in tandem with hyperthermia-induced apoptosis, thereby enhancing overall therapeutic efficacy.[109,131,132]

CDs1 and CDs2 also displayed notable antitumoral effects, albeit slightly lower than CDs3. Their ability to generate $^1O_2$ and increase local temperature under irradiation contributed to their cytotoxicity, demonstrating a synergistic PDT-PTT mechanism. In contrast, CDs4 exhibited minimal singlet oxygen generation and weaker photothermal effects, resulting in reduced antitumoral activity. This suggests that the structural properties of CDs, including aromaticity and surface functionalization, play a crucial role in determining their effectiveness in cancer therapy.

Overall, these results demonstrate that CDs3, followed by CDs1 and CDs2, possess significant photodynamic and photothermal properties that can be leveraged for antitumoral applications. Their ability to generate ROS, induce oxidative stress, and achieve localized hyperthermia under irradiation positions them as promising candidates for PDT and PTT in both bacterial infections and cancer treatment.[132,133]

Conclusions

CDs were synthesized from natural green carbon sources of annatto, cinnamon, curcumin, and sucrose. The obtained CDs products were identified as CDs1, CDs2, CDs3, and CDs4. CD particle size showed a diameter mean size of 2.30 nm. Regarding the chemical composition by FTIR analyses, hydroxyls, amines, and carboxyl functionalized groups promote antimicrobial and antitumoral capacities. The CDs´s cytotoxicity was evaluated against monkey kidney cells, and it was confirmed that the employed concentration of 2000 $\mu g \cdot mL^{-1}$ was lower than that of the IC50 at 24 h (<5000 $\mu g \cdot mL^{-1}$). The antibacterial capacity of the CDs was positively verified against microorganism *methicillin-resistant S. aureus* (*MRSA*) and *Extended-Spectrum β-Lactamase (ESBL)-producing E. coli* since complete inhibition was achieved after blue light irradiation (450 nm; 40 $mW \cdot cm^{-2}$). Concerning PTT characteristics in all cases, there was evidence of an increment in temperature over 40 °C after 30 min of irradiation. Finally, the antitumoral properties of CDs3 were successfully evaluated against T-47D cells (human breast cancer cell line).

This study demonstrated that is viable to employ CDs1, CDs2, CDs3 and CDs4 as photosensitizers (PS) or photothermal agents (PA) within PDT and PTT strategies for antibacterial and antitumoral applications. This approach can be used in the future for bacterial and tumor elimination in the dermatological area. In addition, we proved that the employed carbon sources (*Bixa Orellana L., Cinnamomum verum J. Presl*, and *Curcuma longa L)*. can be used to develop antibacterial/antitumor nanomedicine, despite some differences could appear in the natural extracts due to the obtaining process.

Acknowledgment

All the authors want to thanks to Dr. Jaime A. Costales, CISeAL Director for having provided the LLC-MK2 cells. In addition, we thanks to the Research Directorate of PUCE. The authors thank the Research Directorate of the Pontifical Catholic University of Ecuador (PUCE) for funding the publication costs of this article.

Author Contributions

All authors made a significant contribution to the work reported, whether that is in the conception, study design, execution, acquisition of data, analysis and interpretation, or in all these areas; took part in drafting, revising or critically reviewing the article; gave final approval of the version to be published; have agreed on the journal to which the article has been submitted; and agree to be accountable for all aspects of the work.

Disclosure

The authors report no conflicts of interest in this work.

References

1. Benjamin SR, Ribeiro Júnior EJM, de Andrade GM, Oriá RB. Zero-dimensional carbon nanomaterials for cancer diagnosis. In: *Zero-Dimensional Carbon Nanomaterials*. IOP Publishing; 2022:7–14. doi:10.1088/978-0-7503-4048-9ch7
2. Beura R, Tyagi M, Mohapatra S. The physical and luminescent properties of zero-dimensional carbon nanomaterials. In: *Zero-Dimensional Carbon Nanomaterials*. IOP Publishing;2022:3–14. doi:10.1088/978-0-7503-4048-9ch3
3. Lagos KJ, García D, Cuadrado CF, et al. Carbon dots: types, preparation, and their boosted antibacterial activity by photoactivation. Current status and future perspectives. *Wiley Interdiscip Rev Nanomed Nanobiotechnol*. 2023:1–29. doi:10.1002/wnan.1887
4. Li S, Li L, Tu H, et al. The development of carbon dots: from the perspective of materials chemistry. *Mater Today*. 2021;51 (December):188–207. doi:10.1016/j.mattod.2021.07.028
5. Park Y, Yoo J, Lim B, Kwon W, Rhee SW. Improving the functionality of carbon nanodots: doping and surface functionalization. *J Mater Chem a Mater*. 2016;4(30):11582–11603. doi:10.1039/c6ta04813g
6. Kochkar H, Lakhdhar N, Berhault G, Bausach M, Abdelhamid G. Optimization of the alkaline hydrothermal route to titanate nanotubes by a doehlert matrix experience design. *J Phys Chem C*. 2009;113(5):1672–1679. doi:10.1021/jp809131z
7. De Medeiros TV, Manioudakis J, Noun F, Macairan JR, Victoria F, Naccache R. Microwave-assisted synthesis of carbon dots and their applications. *J Mater Chem C Mater*. 2019;7(24):7175–7195. doi:10.1039/c9tc01640f
8. Zhang X, Liu C, Li Z, et al. An easily prepared carbon quantum dots and employment for inverted organic photovoltaic devices. *Chem Eng J*. 2017;315:621–629. doi:10.1016/j.cej.2017.01.067
9. Martins NCT, Ângelo J, Girão AV, Trindade T, Andrade L, Mendes A. N-doped carbon quantum dots/TiO2 composite with improved photocatalytic activity. *Appl Catal: B*. 2016;193:67–74. doi:10.1016/j.apcatb.2016.04.016
10. Qin X, Lu W, Asiri AM, Al-Youbi AO, Sun X. Microwave-assisted rapid green synthesis of photoluminescent carbon nanodots from flour and their applications for sensitive and selective detection of mercury(II) ions. *Sens Actuators B Chem*. 2013;184:156–162. doi:10.1016/j.snb.2013.04.079
11. Huang S, Wang L, Zhu F, et al. A ratiometric nanosensor based on fluorescent carbon dots for label-free and highly selective recognition of DNA. *RSC Adv*. 2015;5(55):44587–44597. doi:10.1039/C5RA05519A
12. Lee HU, Park SY, Park ES, et al. Photoluminescent carbon nanotags from harmful cyanobacteria for drug delivery and imaging in cancer cells. *Sci Rep*. 2014;4(1):4665. doi:10.1038/srep04665
13. Zhao P, Xu Q, Tao J, et al. Near infrared quantum dots in biomedical applications: current status and future perspective. *Wiley Interdiscip Rev Nanomed Nanobiotechnol*. 2018;10(3):e1483. doi:10.1002/wnan.1483
14. Atchudan R, Edison TNJI, Perumal S, Vinodh R, Lee YR. Betel-derived nitrogen-doped multicolor carbon dots for environmental and biological applications. *J Mol Liq*. 2019;296:111817. doi:10.1016/j.molliq.2019.111817
15. Atchudan R, Edison TNJI, Aseer KR, Perumal S, Karthik N, Lee YR. Highly fluorescent nitrogen-doped carbon dots derived from Phyllanthus acidus utilized as a fluorescent probe for label-free selective detection of Fe3+ ions, live cell imaging and fluorescent ink. *Biosens Bioelectron*. 2018;99:303–311. doi:10.1016/j.bios.2017.07.076
16. Atchudan R, Chandra Kishore S, Gangadaran P, et al. Tunable fluorescent carbon dots from biowaste as fluorescence ink and imaging human normal and cancer cells. *Environ Res*. 2022;204:112365. doi:10.1016/j.envres.2021.112365
17. Meng W, Bai X, Wang B, Liu Z, Lu S, Yang B. Biomass-derived carbon dots and their applications. *Energy Environ Mater*. 2019;2(3):172–192. doi:10.1002/eem2.12038
18. Jorns M, Pappas D. A review of fluorescent carbon dots, their synthesis, physical and chemical characteristics, and applications. *Nanomaterials*. 2021;11(6):1448. doi:10.3390/nano11061448
19. Atchudan R, Edison TNJI, Mani S, et al. Facile synthesis of a novel nitrogen-doped carbon dot adorned zinc oxide composite for photodegradation of methylene blue. *Dalton Trans*. 2020;49(48):17725–17736. doi:10.1039/D0DT02756A
20. HKM N, Lim GK, Leo CP. Comparison between hydrothermal and microwave-assisted synthesis of carbon dots from biowaste and chemical for heavy metal detection: a review. *Microchem J*. 2021;165:106116. doi:10.1016/j.microc.2021.106116
21. Bavykin DV, Kulak AN, Walsh FC. Metastable nature of titanate nanotubes in an alkaline environment. *Cryst Growth Des*. 2010;10 (10):4421–4427. doi:10.1021/cg100529y
22. Sahu S, Behera B, Maiti TK, Mohapatra S. Simple one-step synthesis of highly luminescent carbon dots from orange juice: application as excellent bio-imaging agents. *Chem Commun*. 2012;48(70):8835–8837. doi:10.1039/c2cc33796g
23. Bag P, Maurya RK, Dadwal A, et al. Recent development in synthesis of carbon dots from natural resources and their applications in biomedicine and multi-sensing platform. *ChemistrySelect*. 2021;6(11):2774–2789. doi:10.1002/slct.202100468
24. Humaera NA, Fahri AN, Armynah B, Tahir D. Natural source of carbon dots from part of a plant and its applications: a review. *Luminescence*. 2021;36(6):1354–1364. doi:10.1002/bio.4084
25. Atchudan R, Edison TNJI, Perumal S, Muthuchamy N, Lee YR. Hydrophilic nitrogen-doped carbon dots from biowaste using dwarf banana peel for environmental and biological applications. *Fuel*. 2020;275:117821. doi:10.1016/j.fuel.2020.117821
26. Viuda-Martos M, Ciro-Gómez GL, Ruiz-Navajas Y, et al. In vitro antioxidant and antibacterial activities of extracts from annatto (Bixa orellana L.) leaves and seeds. *J Food Saf*. 2012;32(4):399–406. doi:10.1111/j.1745-4565.2012.00393.x
27. Vasconcelos NG, Croda J, Simionatto S. Antibacterial mechanisms of cinnamon and its constituents: a review. *Microb Pathog*. 2018;120:198–203. doi:10.1016/j.micpath.2018.04.036
28. Zhang Y, Liu X, Wang Y, Jiang P, Quek S. Antibacterial activity and mechanism of cinnamon essential oil against Escherichia coli and Staphylococcus aureus. *Food Control*. 2016;59:282–289. doi:10.1016/j.foodcont.2015.05.032
29. Roy S, Priyadarshi R, Ezati P, Rhim JW. Curcumin and its uses in active and smart food packaging applications - a comprehensive review. *Food Chem*. 2022;375:131885. doi:10.1016/j.foodchem.2021.131885

30. Hettiarachchi SS, Perera Y, Dunuweera SP, Dunuweera AN, Rajapakse S, Rajapakse RMG. Comparison of antibacterial activity of nanocurcumin with bulk curcumin. *ACS Omega*. 2022;7(50):46494–46500. doi:10.1021/acsomega.2c05293
31. Arul V, Radhakrishnan K, Sampathkumar N, Vinoth Kumar J, Abirami N, Inbaraj BS. Detoxification of toxic organic dye by heteroatom-doped fluorescent carbon dots prepared by green hydrothermal method using garcinia mangostana extract. *Agronomy*. 2023;13(1):205. doi:10.3390/agronomy13010205
32. Deng WW, Zang CR, Li QC, et al. Hydrothermally derived green carbon dots from broccoli water extracts: decreased toxicity, enhanced free-radical scavenging, and anti-inflammatory performance. *ACS Biomater Sci Eng*. 2023;9(3):1307–1319. doi:10.1021/acsbiomaterials.2c01537
33. García DG, Garzón-Romero C, Salazar MA, et al. Bioinspired synthesis of magnetic nanoparticles based on iron oxides using orange waste and their application as photo-activated antibacterial agents. *Int J Mol Sci*. 2023;24(5):4770. doi:10.3390/ijms24054770
34. Zhang X, Jiang M, Niu N, et al. Natural-product-derived carbon dots: from natural products to functional materials. *ChemSusChem*. 2018;11(1):11–24. doi:10.1002/cssc.201701847
35. Liu ML, Chen BB, Li CM, Huang CZ. Carbon dots: synthesis, formation mechanism, fluorescence origin and sensing applications. *Green Chem*. 2019;21(3):449–471. doi:10.1039/c8gc02736f
36. Varsha Raveendran PT, Renuka NK. Carbon dots as a sustainable alternative to plant extracts for the green synthesis of noble metal nanoparticles. *Environ Nanotechnol Monit Manag*. 2022;18:100676. doi:10.1016/j.enmm.2022.100676
37. Lin X, Xiong M, Zhang J, et al. Carbon dots based on natural resources: synthesis and applications in sensors. *Microchem J*. 2021;160(PA):105604. doi:10.1016/j.microc.2020.105604
38. Handayani I, Haryanti P, Sulistyo SB. Color and antibacterial activity of annatto extracts at various pH of distilled water solvent and extraction temperature. *Food Res*. 2021;5(6):247–253. doi:10.26656/fr.2017.5(6).740
39. Yolmeh M, Habibi Najafi MB, Farhoosh R, Salehi F. Modeling of antibacterial activity of annatto dye on Escherichia coli in mayonnaise. *Food Biosci*. 2014;8:8–13. doi:10.1016/j.fbio.2014.09.001
40. Nabavi SF, Di Lorenzo A, Izadi M, Sobarzo-Sánchez E, Daglia M, Nabavi SM. Antibacterial effects of cinnamon: from farm to food, cosmetic and pharmaceutical industries. *Nutrients*. 2015;7(9):7729–7748. doi:10.3390/nu7095359
41. Zorofchian Moghadamtousi S, Abdul Kadir H, Hassandarvish P, Tajik H, Abubakar S, Zandi K. A review on antibacterial, antiviral, and antifungal activity of curcumin. *Biomed Res Int*. 2014;2014:186864. doi:10.1155/2014/186864
42. Teow SY, Liew K, Ali SA, Khoo ASB, Peh SC. Antibacterial action of curcumin against *Staphylococcus aureus*: a brief review. *J Trop Med*. 2016;2016:2853045. doi:10.1155/2016/2853045
43. Ullal N, Muthamma K, Sunil D. Carbon dots from eco-friendly precursors for optical sensing application: an up-to-date review. *Chem Papers*. 2022;76(10):6097–6127. doi:10.1007/s11696-022-02353-3
44. Rodríguez-Varillas S, Fontanil T, Obaya ÁJ, Fernández-González A, Murru C, Badía-Laíño R. Biocompatibility and antioxidant capabilities of carbon dots obtained from tomato (Solanum lycopersicum). *Appl Sci*. 2022;12(2):773. doi:10.3390/app12020773
45. Mathew S, Thara CR, John N, Mathew B. Carbon dots from green sources as efficient sensor and as anticancer agent. *J Photochem Photobiol A*. 2023;434:114237. doi:10.1016/j.jphotochem.2022.114237
46. Liu M. Optical properties of carbon dots: a review. *Nanoarchitectonics*. 2020;1(1):1–12. doi:10.37256/nat.112020124.1-12
47. Ge G, Li L, Wang D, et al. Carbon dots: synthesis{,} properties and biomedical applications. *J Mater Chem B*. 2021;9(33):6553–6575. doi:10.1039/D1TB01077H
48. Balou S, Shandilya P, Priye A. Carbon dots for photothermal applications. *Front Chem*. 2022;10. doi:10.3389/fchem.2022.1023602
49. Getachew G, Korupalli C, Rasal AS, Chang JY. ROS generation/scavenging modulation of carbon dots as phototherapeutic candidates and peroxidase mimetics to integrate with polydopamine nanoparticles/GOx towards cooperative cancer therapy. *Compos B Eng*. 2021;226:109364. doi:10.1016/j.compositesb.2021.109364
50. Wang B, Lu S. The light of carbon dots: from mechanism to applications. *Matter*. 2022;5(1):110–149. doi:10.1016/j.matt.2021.10.016
51. Giancarlo García Vélez D, Janneri Lagos Álvarez K, Paulina Romero Obando M. *Antibacterial Strategies: Photodynamic and Photothermal Treatments Based on Carbon-Based Materials*. In: Villarreal-Gómez D, editor. IntechOpen; 2023:Ch.11. doi:10.5772/intechopen.109780
52. Lagos KJ, Buzzá HH, Bagnato VS, Romero MP. Carbon-based materials in photodynamic and photothermal therapies applied to tumor destruction. *Int J Mol Sci*. 2022;23(1). doi:10.3390/ijms23010022
53. Kamaruzzaman NF, Kendall S, Good L. Targeting the hard to reach: challenges and novel strategies in the treatment of intracellular bacterial infections. *Br J Pharmacol*. 2017;174(14):2225–2236. doi:10.1111/bph.13664
54. Cano A, Ettcheto M, Espina M, et al. State-of-the-art polymeric nanoparticles as promising therapeutic tools against human bacterial infections. *J Nanobiotechnology*. 2020;18(1):156. doi:10.1186/s12951-020-00714-2
55. Poolman JT, Anderson AS. Escherichia coli and Staphylococcus aureus: leading bacterial pathogens of healthcare associated infections and bacteremia in older-age populations. *Expert Rev Vaccines*. 2018;17(7):607–618. doi:10.1080/14760584.2018.1488590
56. Wang Y, Jin Y, Chen W, et al. Construction of nanomaterials with targeting phototherapy properties to inhibit resistant bacteria and biofilm infections. *Chem Eng J*. 2019;358(September 2018):74–90. doi:10.1016/j.cej.2018.10.002
57. de Kraker MEA, Davey PG, Grundmann H. Mortality and hospital stay associated with resistant Staphylococcus aureus and Escherichia coli bacteremia: estimating the burden of antibiotic resistance in Europe. *PLoS Med*. 2011;8(10):e1001104. doi:10.1371/journal.pmed.1001104
58. Wu X, Abbas K, Yang Y, Li Z, Tedesco AC. Photodynamic anti-bacteria by carbon dots and their nano composites. *Pharmaceuticals*. 2022:1–21. doi:10.3390/ph15040487
59. Chu X, Zhang P, Wang Y, et al. Near-infrared carbon dot-based platform for bioimaging and photothermal/photodynamic/quaternary ammonium triple synergistic sterilization triggered by single NIR light source. *Carbon N Y*. 2021;176:126–138. doi:10.1016/j.carbon.2021.01.119
60. Lv Y, Li P, Su R, et al. Methylene blue/carbon dots composite with photothermal and photodynamic properties: synthesis, characterization, and antibacterial application. *Photochem Photobiol*. 2023;99(1):92–100. doi:10.1111/php.13680
61. Kandil AA, Elhadidy M, El-Gamal A, Al-Ashmawy MA. Identification of S. aureus and E. coli from dairy products intended for human consumption. *Adv Anim Vet Sci*. 2018;6(11):509–513. doi:10.17582/journal.aavs/2018/6.11.509.513
62. Alzaben F, Fat'hi S, Elbehiry A, et al. Laboratory diagnostic methods and antibiotic resistance patterns of Staphylococcus aureus and Escherichia coli strains: an evolving human health challenge. *Diagnostics*. 2022;12(11):2645. doi:10.3390/diagnostics12112645

63. Qi J, Zhang R, Liu X, et al. Carbon dots as advanced drug-delivery nanoplatforms for antiinflammatory, antibacterial, and anticancer applications: a review. *ACS Appl Nano Mater*. 2023;6(11):9071–9084. doi:10.1021/acsanm.3c01207
64. Muktha H, Sharath R, Kottam N, Smrithi SP, Samrat K, Ankitha P. Green synthesis of carbon dots and evaluation of its pharmacological activities. *Bionanoscience*. 2020;10(3):731–744. doi:10.1007/s12668-020-00741-1
65. Niu G, Gao F, Li C, Wang Y, Li H, Jiang Y. Dual enzyme-mimicking carbon dots for enhanced antibacterial activity. *J Mater Chem B*. 2023;11 (37):8916–8925. doi:10.1039/D3TB01376F
66. Yan H, Zhang B, Zhang Y, Su R, Li P, Su W. Fluorescent carbon dot-curcumin nanocomposites for remarkable antibacterial activity with synergistic photodynamic and photothermal abilities. *ACS Appl Bio Mater*. 2021;4(9):6703–6718. doi:10.1021/acsabm.1c00377
67. Wen F, Li P, Meng H, et al. Nitrogen-doped carbon dots/curcumin nanocomposite for combined Photodynamic/photothermal dual-mode antibacterial therapy. *Photodiagnosis Photodyn Ther*. 2022:39. doi:10.1016/j.pdpdt.2022.103033
68. Mei L, Gao X, Shi Y, et al. Augmented graphene quantum dot-light irradiation therapy for bacteria-infected wounds. *ACS Appl Mater Interfaces*. 2020;12(36):40153–40162. doi:10.1021/acsami.0c13237
69. Naskar A, Kim KS. Friends against the foe: synergistic photothermal and photodynamic therapy against bacterial infections. *Pharmaceutics*. 2023;15(4):1116. doi:10.3390/pharmaceutics15041116
70. Miller KD, Nogueira L, Mariotto AB, et al. Cancer treatment and survivorship statistics, 2019. *CA Cancer J Clin*. 2019;69(5):363–385. doi:10.3322/caac.21565
71. Dos Santos AF, De Almeida DRQ, Terra LF, Baptista MS, Labriola L. Photodynamic therapy in cancer treatment - an update review. *J Cancer Metastasis Treat*. 2019;2019. doi:10.20517/2394-4722.2018.83
72. Liu Y, Bhattarai P, Dai Z, Chen X. Photothermal therapy and photoacoustic imaging: via nanotheranostics in fighting cancer. *Chem Soc Rev*. 2019;48(7):2053–2108. doi:10.1039/c8cs00618k
73. Yue J, Miao P, Li L, Yan R, Dong WF, Mei Q. Injectable carbon dots-based hydrogel for combined photothermal therapy and photodynamic therapy of cancer. *ACS Appl Mater Interfaces*. 2022;14(44):49582–49591. doi:10.1021/acsami.2c15428
74. Zhang M, Wang W, Wu F, et al. Biodegradable Poly(γ-glutamic acid)@glucose oxidase@carbon dot nanoparticles for simultaneous multimodal imaging and synergetic cancer therapy. *Biomaterials*. 2020;252:120106. doi:10.1016/j.biomaterials.2020.120106
75. Das R, Bandyopadhyay R, Pramanik P. Carbon quantum dots from natural resource: a review. *Mater Today Chem*. 2018;8:96–109. doi:10.1016/j.mtchem.2018.03.003
76. Nie H, Li M, Li Q, et al. Carbon dots with continuously tunable full-color emission and their application in ratiometric pH sensing. *Chem Mater*. 2014;26(10):3104–3112. doi:10.1021/cm5003669
77. Yang M, Meng X, Li B, Ge S, Lu Y. N, S co-doped carbon dots with high quantum yield: tunable fluorescence in liquid/solid and extensible applications. *J Nanopart Res*. 2017;19:1–12. doi:10.1007/s11051-017-3914-7
78. Diwan I, Tripathi GK, Khare PS. Synthesis of green fluorescent, energy efficient nitrogen doped carbon quantum dots. *Optik*. 2024;303:171725. doi:10.1016/j.ijleo.2024.171725
79. Herbani Y, Suliyanti MM, Suliyanti MM. Concentration effect on optical properties of carbon dots at room temperature. *J Lumin*. 2018;198:215–219. doi:10.1016/j.jlumin.2018.02.012
80. Vasimalai N, Vilas-Boas V, Gallo J, et al. Green synthesis of fluorescent carbon dots from spices for in vitro imaging and tumour cell growth inhibition. *Beilstein J Nanotechnol*. 2018;9(1):530–544. doi:10.3762/bjnano.9.51
81. Ghann W, Sharma V, Kang H, et al. The synthesis and characterization of carbon dots and their application in dye sensitized solar cell. *Int J Hydrogen Energy*. 2019;44(29):14580–14587. doi:10.1016/j.ijhydene.2019.04.072
82. Sahiner N, Suner SS, Sahiner M, Silan C. Nitrogen and sulfur doped carbon dots from amino acids for potential biomedical applications. *J Fluoresc*. 2019;29(5):1191–1200. doi:10.1007/s10895-019-02431-y
83. Hua XW, Bao YW, Wang HY, Chen Z, Wu FG. Bacteria-derived fluorescent carbon dots for microbial live/dead differentiation. *Nanoscale*. 2017;9(6):2150–2161. doi:10.1039/C6NR06558A
84. Konkena B, Vasudevan S. Understanding aqueous dispersibility of graphene oxide and reduced graphene oxide through p K a measurements. *J Phys Chem Lett*. 2012;3(7):867–872. doi:10.1021/jz300236w
85. Hatimuria M, Phukan P, Bag S, et al. Green carbon dots: applications in development of electrochemical sensors, assessment of toxicity as well as anticancer properties. *Catalysts*. 2023;13(3):537. doi:10.3390/catal13030537
86. Khairol Anuar NK, Tan HL, Lim YP, So'aib MS, Abu Bakar NF. A review on multifunctional carbon-dots synthesized from biomass waste: design/ fabrication, characterization and applications. *Front Energy Res*. 2021;9. doi:10.3389/fenrg.2021.626549
87. Mewada A, Pandey S, Shinde S, et al. Green synthesis of biocompatible carbon dots using aqueous extract of Trapa bispinosa peel. *Mater Sci Eng*. 2013;33(5):2914–2917. doi:10.1016/j.msec.2013.03.018
88. Hao Y, Gan Z, Zhu X, Li T, Wu X, Chu PK. Emission from trions in carbon quantum dots. *J Phys Chem C*. 2015;119(6):2956–2962. doi:10.1021/jp5114569
89. Li M, Yu C, Hu C, et al. Solvothermal conversion of coal into nitrogen-doped carbon dots with singlet oxygen generation and high quantum yield. *Chem Eng J*. 2017;320:570–575. doi:10.1016/j.cej.2017.03.090
90. Li H, He X, Kang Z, et al. Water-soluble fluorescent carbon quantum dots and photocatalyst design. *Angew Chem Int Ed*. 2010;49 (26):4430–4434. doi:10.1002/anie.200906154
91. Zhang H, Huang H, Ming H, et al. Carbon quantum dots/Ag 3 PO 4 complex photocatalysts with enhanced photocatalytic activity and stability under visible light. *J Mater Chem*. 2012;22(21):10501–10506. doi:10.1039/c2jm30703k
92. Kun WU, Si-zhe XU, Xue-jiao Z, Hai-xia WU. Graphene quantum dots enhanced electrochemical performance of polypyrrole as supercapacitor electrode. *J Electrochemist*. 2013;19(4):361.
93. Wang Q, Zhang C, Shen G, Liu H, Fu H, Cui D. Fluorescent carbon dots as an efficient siRNA nanocarrier for its interference therapy in gastric cancer cells. *J Nanobiotechnology*. 2014;12(1):1–12. doi:10.1186/s12951-014-0058-0
94. Fan T, Zeng W, Tang W, et al. Controllable size-selective method to prepare graphene quantum dots from graphene oxide. *Nanoscale Res Lett*. 2015;10:1–8. doi:10.1186/s11671-015-0783-9

95. Hamishehkar H, Ghasemzadeh B, Naseri A, Salehi R, Rasoulzadeh F. Carbon dots preparation as a fluorescent sensing platform for highly efficient detection of Fe(III) ions in biological systems. *Spectrochim Acta A Mol Biomol Spectrosc*. 2015;150:934–939. doi:10.1016/j.saa.2015.06.061
96. Kung JC, Tseng IT, Chien CS, Lin SH, Wang CC, Shih CJ. Microwave assisted synthesis of negative-charge carbon dots with potential antibacterial activity against multi-drug resistant bacteria. *RSC Adv*. 2020;10(67):41202–41208. doi:10.1039/d0ra07106d
97. De B, Karak N. A green and facile approach for the synthesis of water soluble fluorescent carbon dots from banana juice. *RSC Adv*. 2013;3(22):8286–8290. doi:10.1039/c3ra00088e
98. Nguyen HY, Le XH, Dao NT, et al. Microwave-assisted synthesis of graphene quantum dots and nitrogen-doped graphene quantum dots: raman characterization and their optical properties. *Adv Nat Sci*. 2019;10(2). doi:10.1088/2043-6254/ab1b73
99. Dresselhaus MS, Jorio A, Souza Filho AG, Saito R. Defect characterization in graphene and carbon nanotubes using Raman spectroscopy. *Philos Trans Royal Soc A*. 2010;368(1932):5355–5377. doi:10.1098/rsta.2010.0213
100. Gong X, Lu W, Paau MC, et al. Facile synthesis of nitrogen-doped carbon dots for Fe3+ sensing and cellular imaging. *Anal Chim Acta*. 2015;861:74–84. doi:10.1016/j.aca.2014.12.045
101. da Silva Souza DR, Caminhas LD, de Mesquita JP, Pereira FV. Luminescent carbon dots obtained from cellulose. *Mater Chem Phys*. 2018;203:148–155. doi:10.1016/j.matchemphys.2017.10.001
102. Varghese M, Balachandran M. Antibacterial efficiency of carbon dots against Gram-positive and Gram-negative bacteria: a review. *J Environ Chem Eng*. 2021;9(6):106821. doi:10.1016/j.jece.2021.106821
103. van Dam B, Nie H, Ju B, et al. Excitation-dependent photoluminescence from single-carbon dots. *Small*. 2017;13(48):1–5. doi:10.1002/smll.201702098
104. Ai L, Yang Y, Wang B, et al. Insights into photoluminescence mechanisms of carbon dots: advances and perspectives. *Sci Bull*. 2021;66(8):839–856. doi:10.1016/j.scib.2020.12.015
105. Tepliakov NV, Kundelev EV, Khavlyuk PD, et al. Sp2-sp3-hybridized atomic domains determine optical features of carbon dots. *ACS Nano*. 2019;13(9):10737–10744. doi:10.1021/acsnano.9b05444
106. Shimojo Y, Nishimura T, Hazama H, Ozawa T, Awazu K. Measurement of absorption and reduced scattering coefficients in Asian human epidermis, dermis, and subcutaneous fat tissues in the 400- to 1100-nm wavelength range for optical penetration depth and energy deposition analysis. *J Biomed Opt*. 2020;25(4):045002. doi:10.1117/1.JBO.25.4.045002
107. Plattfaut I, Demir E, Fuchs PC, et al. Characterization of blue light treatment for infected wounds: antibacterial efficacy of 420, 455, and 480 nm light-emitting diode arrays against common skin pathogens versus blue light-induced skin cell toxicity. *Photobiomodul Photomed Laser Surg*. 2021;39(5):339–348. doi:10.1089/photob.2020.4932
108. Wu S, Zhou R, Chen H, Zhang J, Wu P. Highly efficient oxygen photosensitization of carbon dots: the role of nitrogen doping. *Nanoscale*. 2020;12(9):5543–5553. doi:10.1039/c9nr10986b
109. Najaflu M, Shahgolzari M, Bani F, Khosroushahi AY. Green synthesis of near-infrared copper-doped carbon dots from alcea for cancer photothermal therapy. *ACS Omega*. 2022;7(38):34573–34582. doi:10.1021/acsomega.2c04484
110. Pal T, Mohiyuddin S, Packirisamy G. Facile and green synthesis of multicolor fluorescence carbon dots from curcumin: in vitro and in vivo bioimaging and other applications. *ACS Omega*. 2018;3(1):831–843. doi:10.1021/acsomega.7b01323
111. Guo Y, Liu X, Yang C, et al. Synthesis and peroxidase-like activity of cobalt@carbon-dots hybrid material. *ChemCatChem*. 2015;7(16):2467–2474. doi:10.1002/cctc.201500263
112. Wei Z, Zou H, Liu G, et al. Peroxidase-mimicking evodiamine/indocyanine green nanoliposomes for multimodal imaging-guided theranostics for oral squamous cell carcinoma. *Bioact Mater*. 2021;6(7):2144–2157. doi:10.1016/j.bioactmat.2020.12.016
113. Long Y, Wang X, Shen D, Zheng H. Detection of glucose based on the peroxidase-like activity of reduced state carbon dots. *Talanta*. 2016;159:122–126. doi:10.1016/j.talanta.2016.06.012
114. Sun S, Chen Q, Li Y, Yu Y, Li Z, Lin H. Tumor-specific and photothermal-augmented chemodynamic therapy by ferrocene-carbon dot-crosslinked nanoparticles. *SmartMat*. 2022;3(2):311–322. doi:10.1002/smm2.1119
115. Lv Y, Ma M, Huang Y, Xia Y. Carbon dot nanozymes: how to be close to natural enzymes. *Chem a Eur J*. 2019;25(4):954–960. doi:10.1002/chem.201804419
116. Deshmukh S, Deore A, Mondal S. Ultrafast dynamics in carbon dots as photosensitizers: a review. *ACS Appl Nano Mater*. 2021;4(8):7587–7606. doi:10.1021/acsanm.1c01880
117. Li B, Zhao S, Huang L, Wang Q, Xiao J, Lan M. Recent advances and prospects of carbon dots in phototherapy. *Chem Eng J*. 2021;408:127245. doi:10.1016/j.cej.2020.127245
118. Romero MP, Alves F, Stringasci MD, et al. One-pot microwave-assisted synthesis of carbon dots and in vivo and in vitro antimicrobial photodynamic applications. *Front Microbiol*. 2021;12.
119. Lin F, Wang Z, Wu FG. Carbon dots for killing microorganisms: an update since 2019. *Pharmaceuticals*. 2022;15(10). doi:10.3390/ph15101236
120. Dong X, Liang W, Meziani MJ, Sun YP, Yang L. Carbon dots as potent antimicrobial agents. *Theranostics*. 2020;10(2):671. doi:10.7150/THNO.39863
121. Al Awak MM, Wang P, Wang S, Tang Y, Sun YP, Yang L. Correlation of carbon dots' light-activated antimicrobial activities and fluorescence quantum yield. *RSC Adv*. 2017;7(48):30177–30184. doi:10.1039/c7ra05397e
122. Kanwal A, Uzair B, Sajjad S, et al. Synthesis and characterization of carbon dots coated caco3 nanocarrier for levofloxacin against multidrug resistance extended-spectrum beta-lactamase Escherichia coli of urinary tract infection origin. *Microb Drug Resist*. 2021;28(1):106–119. doi:10.1089/mdr.2020.0621
123. Miao Y, Zhang X, Li J, Yang W, Huang X, Lv J. Preparation and photodynamic antibacterial/anticancer effects of ultralong-lifetime room-temperature phosphorescent N-doped carbon dots. *RSC Adv*. 2022;12(32):20481–20491. doi:10.1039/d2ra02251f
124. Xu T, Liu W, Li Z, et al. Photothermal and selective microbial inactivation behaviors of gluconamide-coated IR780 nanoparticles. *Colloids Surf B Biointerfaces*. 2023;222:113126. doi:10.1016/j.colsurfb.2023.113126
125. Marshall D, Bullerman L. Antimicrobial properties of sucrose fatty acid esters. In: Akoh C, editor. *Carbohydrate Polyesters as Fat Substitutes*. 1994:149–167.

126. Zha K, Zhang W, Hu W, et al. Three-step regenerative strategy: multifunctional bilayer hydrogel for combined photothermal/photodynamic therapy to promote drug-resistant bacteria-infected wound healing. *Adv Funct Mater*. 2024;34(2):2308145. doi:10.1002/adfm.202308145
127. Wang Z, Sheng L, Yang X, et al. Natural biomass-derived carbon dots as potent antimicrobial agents against multidrug-resistant bacteria and their biofilms. *Sustainable Mater Technol*. 2023;36:e00584. doi:10.1016/j.susmat.2023.e00584
128. Tiron A, Stan CS, Luta G, et al. Manganese-doped n-hydroxyphthalimide-derived carbon dots—theranostics applications in experimental breast cancer models. *Pharmaceutics*. 2021;13(11):1982. doi:10.3390/pharmaceutics13111982
129. Acharya B, Behera A, Behera S, Moharana S. Carbon quantum dots: a systematic overview of recent developments in synthesis, properties, and novel therapeutic applications. *Inorg Chem Commun*. 2024;165:112492. doi:10.1016/j.inoche.2024.112492
130. Geng B, Yang D, Pan D, et al. NIR-responsive carbon dots for efficient photothermal cancer therapy at low power densities. *Carbon N Y*. 2018;134:153–162. doi:10.1016/j.carbon.2018.03.084
131. Kim D, Jo G, Chae Y, et al. Bioinspired Camellia japonica carbon dots with high near-infrared absorbance for efficient photothermal cancer therapy. *Nanoscale*. 2021;13(34):14426–14434. doi:10.1039/D1NR03999G
132. Han Y, Liu H, Fan M, et al. Near-infrared-II photothermal ultra-small carbon dots promoting anticancer efficiency by enhancing tumor penetration. *J Colloid Interface Sci*. 2022;616:595–604. doi:10.1016/j.jcis.2022.02.083
133. Feng T, Ai X, Ong H, Zhao Y. Dual-responsive carbon dots for tumor extracellular microenvironment triggered targeting and enhanced anticancer drug delivery. *ACS Appl Mater Interfaces*. 2016;8(29):18732–18740. doi:10.1021/acsami.6b06695